Università di Napoli Federico II – Scuola Superiore Meridionale

PhD program in Genomic and Experimental Medicine (GEM)

Revealing a novel FAM134B-calcium axis: redefining the link between ER-phagy and colorectal cancer

A dissertation presented by

Marianna Esposito

in partial fulfillment of the requirements for the degree of

Doctor of Philosophy

in

Genomic and Experimental Medicine (GEM)- 37º Cycle

Supervisor:

Prof. Paolo Grumati, Ph.D

Professor of Histology and Human Embryology
Department of Clinical Medicine and Surgery
University of Naples "Federico II", Naples, Italy
Principal Investigator- Telethon Institute of Genetics and Medicine (TIGEM)

GEM program coordinator:

Prof. Brunella Franco, MD.,
Professor of Medical Genetics
Department of Translational Medicine
University of Naples "Federico II", Naples, Italy
Principal Investigator- Telethon Institute of Genetics and Medicine (TIGEM)

Table of Contents

Abstract

The endoplasmic reticulum (ER) is a multifunctional organelle essential for protein folding, lipid synthesis, and calcium (Ca^{2+}) storage. Its structural and functional integrity relies on selective quality-control mechanisms, among which ER-phagy plays a central role. The ER-phagy receptor FAM134B is crucial for ER membrane remodeling and turnover. Initially identified in colorectal cancer (CRC) under the name JK-1, its specific contribution to CRC pathophysiology has remained elusive.

Here, we explored the molecular and functional role of FAM134B in a panel of CRC cellular models: CCD 841 CoN (non-tumoral), Caco-2, SW480, SW48, and HCT116. Proteomic analyses revealed a consistent and specific interaction between FAM134B and the Ca^{2+} pump ATP2A2/SERCA2, pointing to a mechanistic connection between ER-phagy and Ca^{2+} homeostasis.

To investigate this relationship, we generated FAM134B knockout cell lines. Loss of FAM134B caused an enlarged ER morphology, heightened sensitivity to SERCA inhibition, and enhanced Ca^{2+} release from the ER upon thapsigargin (TG) treatment. These disturbances led to a mitochondrial Ca^{2+} overload, increased ER–mitochondria contact sites, mitochondrial fragmentation, and impaired respiratory capacity. Functionally, FAM134B deficiency triggered a robust activation of the intrinsic apoptotic pathway.

Remarkably, re-expression of FAM134B in knockout cells restored Ca^{2+} dynamics, mitochondria respiration and reduced apoptotic vulnerability.

Altogether, these findings unveil a previously unrecognized role of FAM134B as a key coordinator of Ca^{2+} signaling at the ER-mitochondria interface, essential to maintain organelle integrity and cell survival under stress conditions.

List of Abbreviations

AMPK - AMP-activated protein kinase
ATG - Autophagy-related gene
ATP2A2/SERCA2 - Sarco/Endoplasmic Reticulum Ca^{2+}-ATPase 2
ATL3 - Atlastin-3
BafA1 - Bafilomycin A1
BiCAP - Bimolecular Complementation Affinity Purification
BiP - Binding Immunoglobulin Protein (also known as GRP78)
BRAF - v-Raf murine sarcoma viral oncogene homolog B
Ca^{2+} - Calcium ion
CCD 841 CoN - Human normal colon epithelial cell line
Caco-2 - Human colorectal adenocarcinoma cell line
CCPG1 - Cell-Cycle Progression Gene 1
CALCOCO1 - Calcium Binding and Coiled-Coil Domain Containing Protein 1
CRC - Colorectal Cancer
DAPI - 4',6-diamidino-2-phenylindole
DMSO - Dimethyl sulfoxide
DNA - Deoxyribonucleic acid
ER - Endoplasmic Reticulum
ER-phagy - Endoplasmic Reticulum-selective autophagy
FAM134A - Family with Sequence Similarity 134 Member A
FAM134B - Family with Sequence Similarity 134 Member B
FAM134C - Family with Sequence Similarity 134 Member C
FAP- Familial Adenomatous Polyposis
FIP 200 - FAK family kinase-interacting protein of 200 kDa
GAPDH- Glyceraldehyde 3-phosphate dehydrogenase
GFP - Green Fluorescent Protein
GIMs - GABARAP interacting motifs
HCT116 - Human colorectal carcinoma cell line
HEK293 - Human Embryonic Kidney 293 cells
HNPCC - Hereditary non-polyposis colorectal cancer
IP - Immunoprecipitation
IP3R - Inositol 1,4,5-trisphosphate receptor
ITPR3 - Inositol 1,4,5-trisphosphate receptor type 3
JK-1 - Original name of the FAM134B gene identified in CRC
KO – Knockout
KRAS - Kirsten rat sarcoma viral oncogene homolog
KDEL - Lys-Asp-Glu-Leu ER retention signal
LC3 - Microtubule-associated protein 1A/1B-light chain 3
LIR - LC3 interacting regions
MAMs - Mitochondria-associated membranes
MAPK - Mitogen-Activated Protein Kinase
MCU - Mitochondrial Calcium Uniporter
MMR - Mismatch Repair
MSI - Microsatellite Instability
mTOR - Mechanistic Target of Rapamycin

PBS - Phosphate-buffered saline
PCR - Polymerase Chain Reaction
PI3K - Phosphoinositide 3-Kinase
PIK3CA - Phosphatidylinositol-4,5-bisphosphate 3-kinase catalytic subunit alpha
PLA - Proximity Ligation Assay
REEP5 - Receptor Expression-Enhancing Protein 5
RFP - Red Fluorescent Protein
RHD - Reticulon Homology Domain
RNA - Ribonucleic acid
RTN3 - Reticulon-3
RyR - Ryanodine Receptor
SD - Standard Deviation
SEC62 - Translocation Protein SEC62
SEM - Standard Error of the Mean
SMAD4 - SMAD Family Member 4
SW48 - Human colorectal adenocarcinoma cell line
SW480 - Human colorectal adenocarcinoma cell line
TEX264 - Testis-expressed protein 264
TG - Thapsigargin
TOMM20 - Translocase of the Outer Mitochondrial Membrane 20
TP53 - Tumor Protein p53
UBAC2 - Ubiquitin-associated domain-containing protein 2
ULK1 - Unc-51-like kinase 1
UPR- Unfolded Protein Response
VDAC - Voltage-Dependent Anion Channel
VINCULIN - Cytoskeletal actin-binding protein involved in cell adhesion
VPS - Vacuolar protein sorting
WB - Western Blot
Wnt - Wingless-related integration site
WT - Wild Type

Introduction

1. Autophagy

1.1 Molecular Mechanisms and Role in Cellular Homeostasis

Autophagy is an evolutionarily conserved catabolic process essential for maintaining cellular integrity by degrading and recycling cytoplasmic components via the lysosomal pathway. First described in yeast by Ohsumi and colleagues (1), this process has been recognized as a fundamental mechanism in eukaryotic cells to respond to metabolic stress, organelle damage, and intracellular pathogen infections (2).

Three primary types of autophagy have been characterized in mammalian cells: macroautophagy, microautophagy, and chaperone-mediated autophagy (CMA). In macroautophagy, cytoplasmic material is sequestered within a double-membraned autophagosome that subsequently fuses with the lysosome, enabling enzymatic degradation and recycling of macromolecules (3). Microautophagy involves the direct invagination of the lysosomal membrane to engulf cytoplasmic content (4). CMA is a selective process wherein soluble cytosolic proteins bearing a KFERQ-like motif are recognized by HSC70 and delivered to the lysosomal membrane, where they are translocated through LAMP-2A (5).

While traditionally viewed as a non-selective survival mechanism, autophagy is now known to involve highly specific pathways referred to as selective autophagy, where particular cargo- damaged mitochondria (mitophagy), protein aggregates (aggrephagy), lipid droplets (lipophagy), and even portions of the ER (ER-phagy) are targeted via receptor proteins (6).

1.2 Molecular Regulation and Stages of Macroautophagy

The canonical macroautophagy process unfolds through a series of tightly regulated stages:

Initiation: the process is activated by inhibition of mTORC1 (mechanistic Target of Rapamycin Complex 1) or activation of AMPK under low energy conditions (7). This leads to the activation of the ULK1 complex (ULK1-ATG13-FIP200-ATG101), which translocates to autophagosome formation sites.

Nucleation: ULK1 complex recruits class III phosphatidylinositol 3-kinase (PI3KC3) complex, consisting of VPS34, Beclin-1, VPS15, and ATG14L. This complex generates phosphatidylinositol-3-phosphate (PI3P), marking the site of phagophore formation.

Elongation and expansion: the phagophore membrane elongates through two ubiquitin-like conjugation systems. In particular, ATG12–ATG5–ATG16L1 complex facilitates the lipidation of LC3 (microtubule-associated protein 1 light chain 3) into LC3-II, which stably associates with the autophagosome membrane and serves as a scaffold for receptor recruitment. *Maturation and fusion*: the mature autophagosome fuses with the lysosome through the action of SNARE proteins, RAB7, and lysosomal tethering factors, forming the autolysosome, where cargo degradation occurs (8). *Degradation and recycling*: Lysosomal hydrolases degrade the sequestered contents, and resulting macromolecules (amino acids, fatty acids, sugars) are recycled back to the cytoplasm for reuse (9).

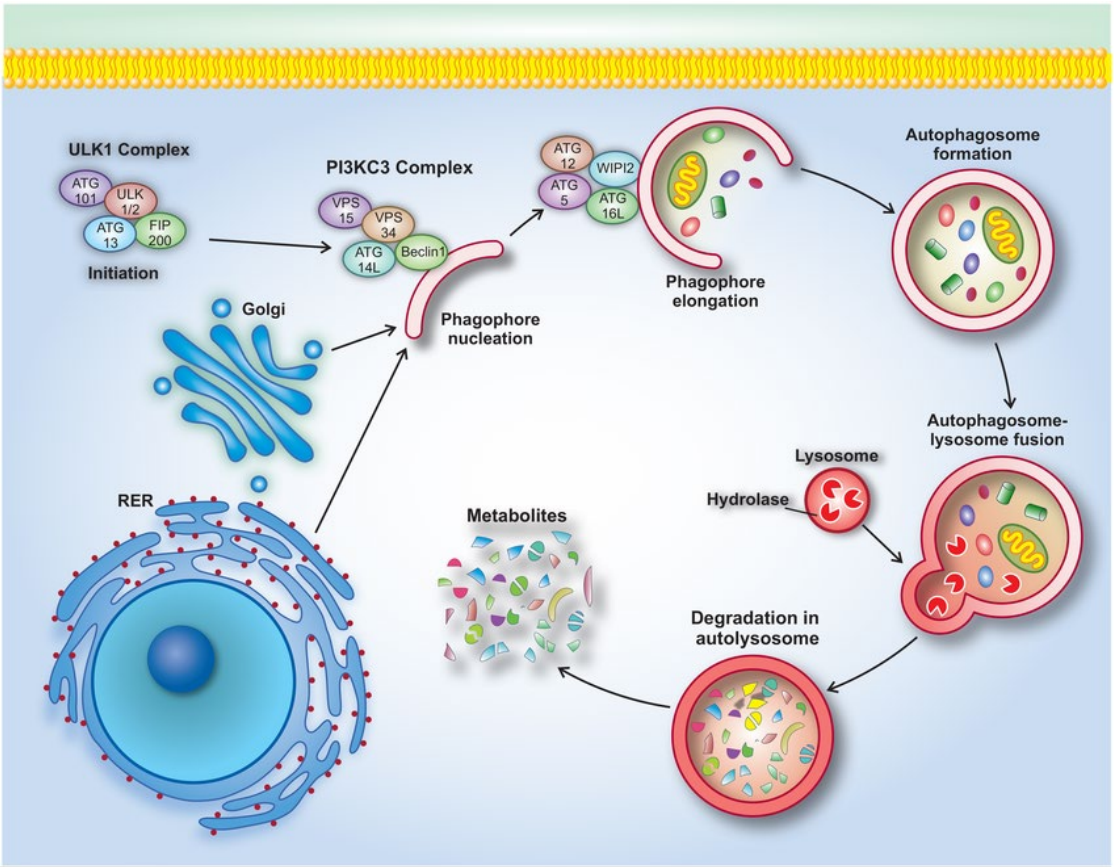

Fig. 1 Representation of the autophagy process that consists of several sequential steps. (1) Initiation. (2) Phagophore nucleation. (3) Phagophore elongation (4) Fusion of autophagosome with lysosome and degradation of cargo in autolysosome. Ahmadi-Dehlaghi et al. 2023.

1.3 Selective Autophagy and Its Physiological Relevance

Selective autophagy is a tightly regulated catabolic process that ensures the targeted degradation of specific cellular components, thereby safeguarding intracellular homeostasis. Among the various forms of selective autophagy are mitophagy, which

eliminates damaged mitochondria; pexophagy, which removes peroxisomes; lipophagy, which targets lipid droplets; and ribophagy, which degrades ribosomes. (10)
A particularly specialized branch is ER-phagy, which mediates the turnover of damaged or superfluous regions of the ER.(11) ER-phagy relies on membrane-anchored receptors containing a conserved LC3-interacting region (LIR) motif that tethers ER membranes to the autophagosomal machinery. To date, several ER-phagy receptors have been identified, and will be described in more detail in the following sections. Among these, FAM134A/B/C, RTN3, SEC62, CCPG1, TEX264, ATL3, UBAC2, and CALCOCO1, each displaying distinct domain specificities and being activated in response to diverse stress conditions, including the accumulation of misfolded proteins or physiological ER remodeling (12,13).
Like other forms of selective autophagy, ER-phagy depends on cargo-recognizing receptors that simultaneously interact with their substrates and with LC3/GABARAP family proteins through LIR motifs. (11) Canonical examples include p62/SQSTM1, which mediates the clearance of ubiquitinated protein aggregates (14); NIX and BNIP3, which act as mitophagy receptors (15); and FAM134B, CCPG1, and RTN3, which function as key ER-phagy receptors (16-18).
Importantly, selective autophagy is not merely a quality-control mechanism. It also fulfils essential physiological roles in developmental remodelling for example during erythroid maturation in immune defense through xenophagic elimination of intracellular pathogens, and in the regulation of inflammation and antigen presentation. (13). Perturbation of these processes contributes to a wide spectrum of human diseases, including neurodegenerative disorders, infections, autoimmune conditions, and cancer (12).
ER-phagy is typically triggered by ER stress, by the accumulation of unfolded or misfolded proteins, or by alterations in lipid metabolism.(19) Through the dynamic remodeling of ER membranes, this pathway not only maintains protein quality control but also contributes to the regulation of intracellular Ca^{2+} homeostasis. (20) Dysregulation of ER-phagy has been increasingly associated with pathological states such as neurodegeneration, chronic inflammatory disorders, and tumorigenesis. (12)

1.4 The Double-Edged Role of Autophagy in Cancer

Autophagy plays a complex and context-dependent role in cancer biology: Tumor-suppressive in early stages, by removing damaged organelles, reducing

oxidative stress, and maintaining genome integrity. Tumor-promoting in advanced cancers, where cells exploit autophagy to survive hypoxia, nutrient deprivation, and chemotherapy (21). In CRC, autophagy can provide metabolic substrates and support immune evasion. Inhibition of autophagy has shown promise in enhancing the efficacy of conventional therapies, yet systemic inhibition may also promote toxicity and inflammation. A promising avenue is the targeted modulation of selective autophagy, particularly ER-phagy, as a way to shift the balance toward pro-death signaling in tumor cells while sparing healthy tissues (21).

In the following section, we will explore the emerging field of ER-phagy in more detail, outlining the receptors involved and their relevance to cellular stress responses and disease progression.

2. ER-phagy and Its Receptors

2.1 Molecular Mechanisms of ER-phagy

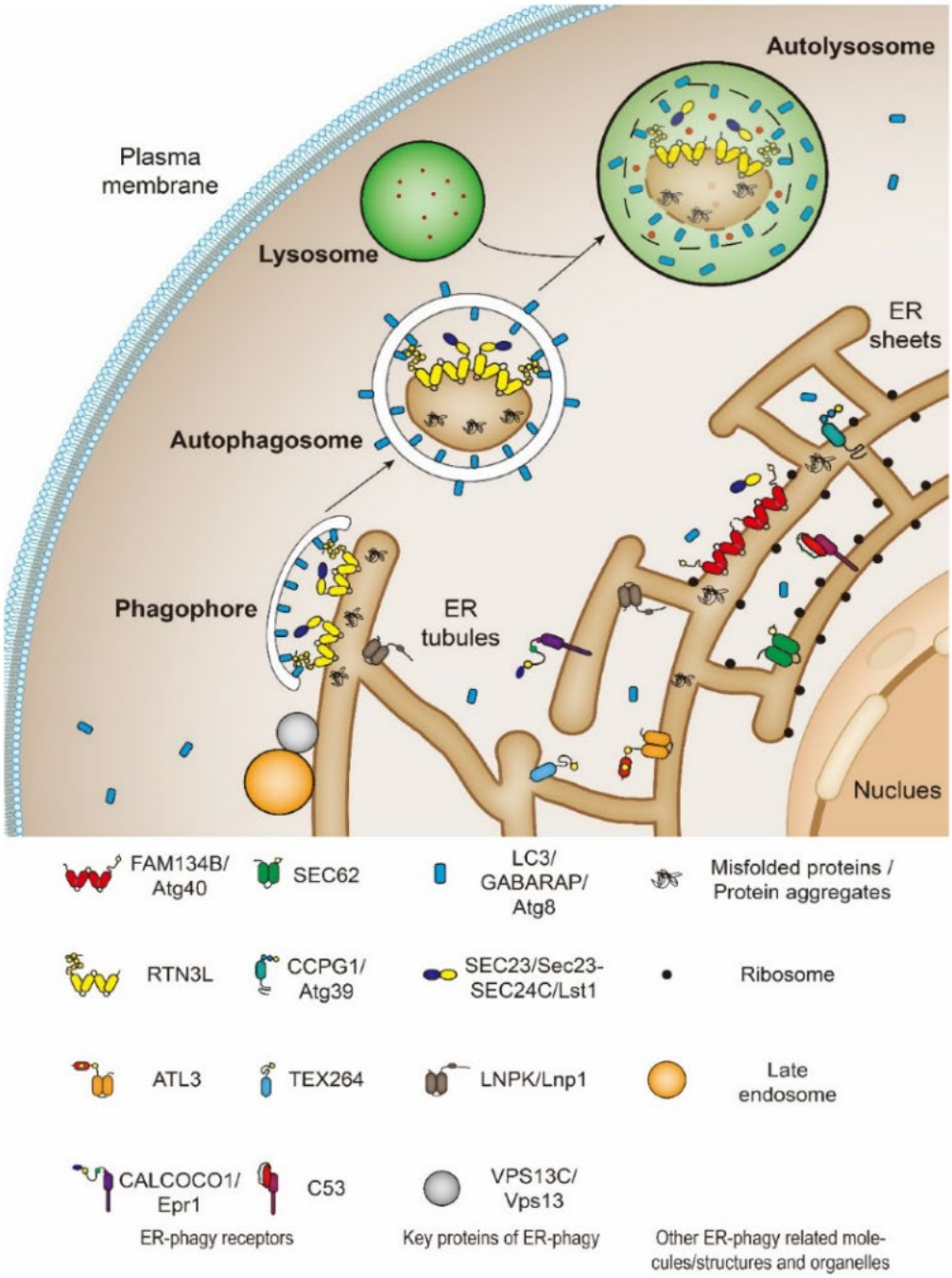

Fig. 2 ER-phagy. Specific ER-phagy receptors cluster at ER subdomains destined for degradation, where they interact with LC3/GABARAP/Atg8 to recruit the autophagic machinery. The phagophore then expands around the ER fragments, sealing to form an autophagosome, which fuses with lysosomes (in mammals) or vacuoles (in yeast and plants) for cargo degradation. He L. et al. 2021.

Selective autophagy of the ER (ER-phagy) is a specialized form of autophagy responsible for the turnover of damaged or excess ER membranes and proteins. It ensures ER homeostasis under both basal and stress conditions, particularly during unfolded protein accumulation, Ca^{2+} dysregulation, or nutrient deprivation. As a subtype of macroautophagy, ER-phagy involves the sequestration of ER fragments into double-membraned autophagosomes that fuse with lysosomes for degradation.

ER-phagy is tightly regulated by the recruitment of autophagy machinery to specific ER subdomains. This recruitment depends on ER-phagy receptors, ER-resident or ER-associated proteins that contain LC3-interacting regions (LIRs) or GABARAP-interacting motifs (GIMs), allowing them to tether ER fragments to ATG8-family proteins on the autophagosomal membrane (12). Receptor activation is often triggered by ER stress signals, such as PERK or IRE1α activation, or by nutrient-sensing pathways like mTORC1 inhibition (12).

Distinct from ER-associated degradation (ERAD), which involves retrotranslocation and proteasomal degradation, ER-phagy mediates bulk degradation of larger ER portions, including sheets or tubules. It plays crucial roles in development, immunity, neurodegeneration, and cancer (22).

2.2 Overview of ER-phagy Receptors

Multiple ER-phagy receptors have been identified in mammals, each associated with different ER subdomains or stress conditions. These receptors include: FAM134A, FAM134B, FAM134B2, FAM134C, RTN3, TEX264, ATL3, SEC62, UBAC2, CALCOCO1, CCPG1. Although they share a common function, linking ER to the autophagic machinery, they differ in expression patterns, structural domains, and stress-responsiveness, suggesting both redundancy and specialization (21,22).

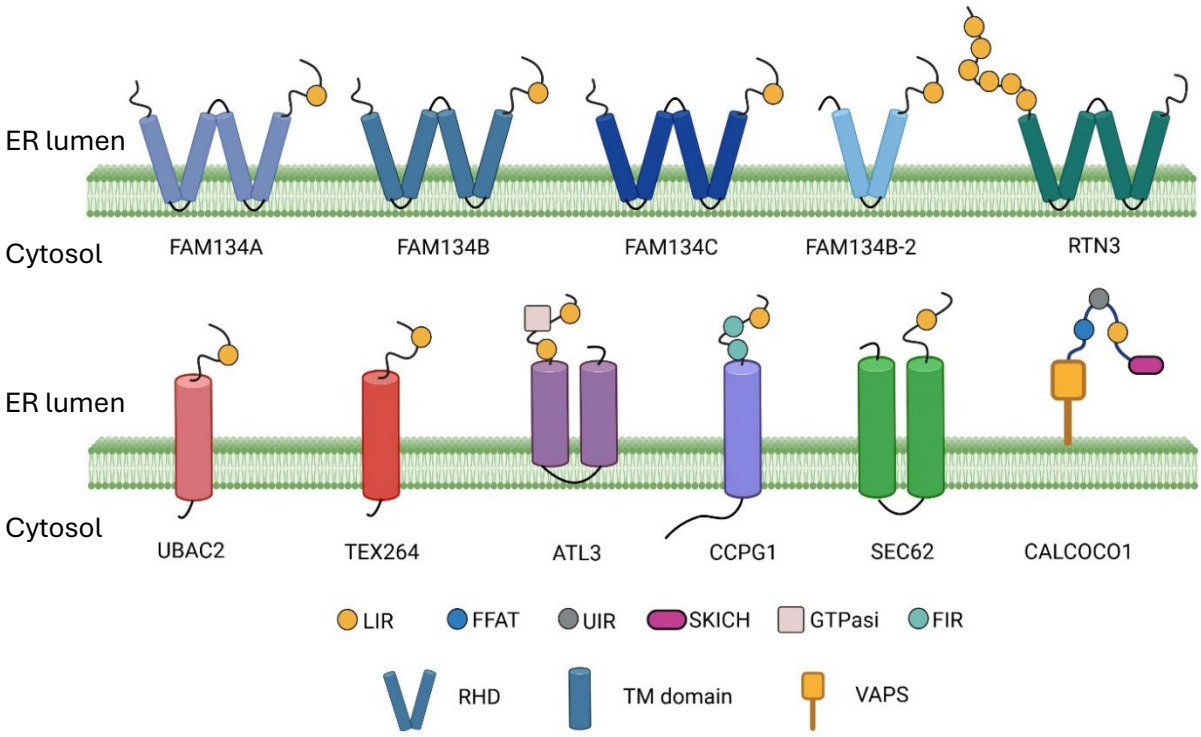

Fig. 3 Detailed structure of ER-phagy Receptors and their various functional domains. Image generated through BioRender.

2.3 FAM134B: A Key ER-phagy Receptor

FAM134B (Family with Sequence Similarity 134 Member B) was the first ER-phagy receptor identified in mammalian cells and remains one of the most extensively studied to date. It localizes to the ER via a conserved reticulon homology domain (RHD), which promotes membrane curvature, and interacts with the autophagy machinery through a canonical LC3-interacting region (LIR) located in its C-terminal cytosolic portion (18).

FAM134B is one of three paralogues FAM134A, FAM134B, and FAM134C that share structural homology yet exert non-redundant roles in ER shaping and selective degradation. Notably, distinct isoforms of FAM134B have been identified: the full-length variant (FAM134B-1), and a shorter isoform (FAM134B-2), recently identified as ER-phagy receptor too (23).

Functionally, FAM134B preferentially regulates sheet-like regions of the ER. Loss of FAM134B disrupts ER homeostasis, leading to ER expansion, activation of the unfolded protein response (UPR), and inefficient degradation of ER-resident proteins. Its physiological relevance is underscored by the fact that biallelic mutations in FAM134B cause hereditary sensory and autonomic neuropathy type II (HSAN-II), a rare neurodegenerative disorder characterized by axonal degeneration in sensory neurons (18).

Beyond its role in neuronal integrity, FAM134B has emerged as a potential modulator of cancer biology. Depending on the cellular context, it may act as a tumor suppressor by promoting the clearance of damaged ER or, conversely, facilitate tumor cell survival under stress conditions by enhancing adaptive ER turnover. Recent comparative analyses of FAM134 paralogues further support their specialized functions in ER remodeling and protein quality control, particularly in relation to collagen biosynthesis and secretion (24). However, the precise role of FAM134B in CRC remains incompletely understood and will be explored in detail in the following sections.

3. CRC: Pathogenesis, ER stress and ER-phagy

3.1 Epidemiology and Risk Factors

CRC is the third most diagnosed malignancy and the second leading cause of cancer-related death worldwide. Its incidence varies by region, being highest in developed countries, reflecting the influence of lifestyle, diet, and screening practices. (25)

Several environmental and genetic risk factors contribute to CRC development. These include high intake of red and processed meat, low fiber consumption, obesity, physical inactivity, alcohol abuse, and smoking (26). Inflammatory bowel diseases, such as ulcerative colitis and Crohn's disease, are also associated with increased CRC risk. On the genetic side, familial adenomatous polyposis (FAP) and Lynch syndrome (hereditary non-polyposis colorectal cancer, HNPCC) are among the most common hereditary syndromes predisposing to CRC (27). Despite advances in early detection and treatment, the prognosis remains poor for advanced-stage CRC, necessitating a deeper understanding of its molecular underpinnings.

3.2 Molecular Pathogenesis and Tumor Progression

CRC arises through a well-defined multistep process of genetic and epigenetic alterations, classically described by the adenoma- carcinoma sequence (25). This model illustrates the progressive accumulation of mutations and chromosomal instability that drive the transition from normal epithelium to adenoma and finally to carcinoma (25).

One of the earliest and most critical alterations occurs in the APC gene, which encodes a key negative regulator of the Wnt/β-catenin signaling pathway. Loss-of-function mutations in APC lead to constitutive activation of Wnt signaling, promoting uncontrolled cellular proliferation and the initiation of adenomas (28).

Subsequent mutations typically include KRAS (activating mutations), which confer growth advantages through the MAPK and PI3K/AKT pathways, and TP53 (tumor suppressor loss), which allows cells with DNA damage to evade apoptosis and continue proliferating (28,29).

In a subset of tumors, particularly those arising through the microsatellite instability (MSI) pathway, defective DNA mismatch repair (MMR) genes such as MLH1, MSH2, MSH6, and PMS2 play a critical role (29). These tumors often have distinct clinicopathological features, including better prognosis and response to immunotherapy.

Other relevant alterations in CRC include mutations in SMAD4 and TGF-β pathway components, affecting epithelial-mesenchymal transition (EMT); PIK3CA, involved in PI3K-AKT-mTOR signaling; and BRAF (especially V600E), associated with poor prognosis and right-sided colon cancer (30).

3.3 The Role of TP53 in Colorectal Cancer

The TP53 gene, often referred to as the "guardian of the genome," encodes the p53 protein, which plays a fundamental role in maintaining genomic stability. Upon DNA damage or cellular stress, p53 is stabilized and activated, leading to cell cycle arrest, senescence, or apoptosis through transcriptional regulation of downstream targets such as BAX, PUMA, and NOXA (31).

In CRC, TP53 mutations occur predominantly in the transition from late adenoma to carcinoma. These mutations result in either loss-of-function or gain-of-function phenotypes that abrogate the tumor suppressive activity of p53. This permits accumulation of additional genetic damage, bypass of apoptosis, and increased resistance to therapy (32) .

Beyond apoptosis, p53 also modulates autophagy in a context-dependent manner. Nuclear p53 can promote autophagy via transcription of autophagy-related genes (e.g., DRAM1, SESN1/2), whereas cytoplasmic p53 may repress it (33). In CRC, the loss of p53 may thus simultaneously reduce apoptotic capacity and deregulate autophagic flux, creating a permissive environment for tumor growth and adaptation to stress conditions, including ER stress and hypoxia (33).

3.4 ER Stress and ER-Phagy in Colorectal Cancer

As tumors grow and outpace their vascular supply, they experience hypoxia, nutrient deprivation, and accumulation of misfolded proteins, which provoke ER stress and activate the UPR. The UPR is a tripartite signaling cascade (IRE1, PERK, ATF6) that aims to restore ER homeostasis or trigger apoptosis if stress remains unresolved (29).

In CRC, chronic ER stress contributes to tumor progression by promoting adaptation and survival. Cells under prolonged stress rely on autophagic mechanisms, particularly ER-phagy, to remove dysfunctional ER components and attenuate proteotoxicity. Among the ER-phagy receptors, FAM134B has garnered particular interest for its role in shaping ER morphology and selectively targeting ER sheets for degradation (34).

FAM134B expression is frequently dysregulated in cancer, with reports indicating both tumor-suppressive and tumor-promoting roles depending on the context (35).

3.5 Therapeutic Targeting of Autophagy and ER-Phagy in CRC

Given the dual role of autophagy in cancer, therapeutic strategies aim to either inhibit or exploit autophagic pathways depending on tumor context and treatment goals. Hydroxychloroquine and related lysosomal inhibitors have been explored in clinical trials as adjuvants to chemotherapy, aiming to block autophagic flux and sensitize cancer cells to stress (34).

Specific targeting of ER-phagy remains in its infancy but shows promise. One approach is to modulate expression or activity of FAM134B and its interacting partners. For example, Chipurupalli et al. demonstrated that cancer cells adapt to hypoxia by regulating BiP, which facilitates FAM134B-mediated ER-phagy, promoting cell survival (36).

Disrupting this axis may represent a novel vulnerability. Inhibitors of BiP or agents that impair LIR-dependent autophagosome recruitment could potentially abrogate ER-phagy in tumor cells.

3.6 Comparative Insights: ER-phagy in Other Tumor Types

The role of ER-phagy in cancer is context-dependent. In liver cancer, FAM134B expression is often reduced, and its overexpression can inhibit proliferation and enhance apoptosis (37). In pancreatic cancer, SEC62-mediated ER-phagy has been implicated in migration and drug resistance (38). In breast cancer, hypoxia triggers ER-phagy through the FAM134B-BiP complex, promoting survival and proliferation; inhibition of FAM134B or BiP reduces tumor growth (36). These studies suggest that modulating ER-phagy could be leveraged to enhance cancer treatment. The growing body of literature underscores that while ER-phagy is a pro-survival mechanism in many tumors, it can also represent a therapeutic vulnerability when dysregulated. Future studies should investigate the differential roles of ER-phagy receptors (e.g., FAM134 family, CCPG1, TEX264, ATL3) across tumor types and stages.

4. ER-phagy and Ca^{2+} Signaling in Colorectal Cancer and Beyond

4.1 ER-phagy, Ca^{2+} Homeostasis, and Cancer Cell Adaptation

Several cancers, including CRC, liver hepatocellular carcinoma, and glioblastoma, display altered expression or activation of ER-phagy receptors (39). In this work, FAM134B has emerged as a potential modulator of processes as apoptosis and Ca^{2+} signaling. The ER serves as a major intracellular Ca^{2+} reservoir, and ER-phagy helps maintain Ca^{2+} homeostasis by removing dysfunctional ER regions that may cause Ca^{2+} leakage or dysregulation (20). Ca^{2+} dysregulation, in turn, can lead to mitochondrial overload, oxidative stress, or the induction of apoptosis via activation of caspases and BAX/BAK-mediated outer mitochondrial membrane permeabilization (40,41). Interestingly, the pro-survival or pro-death outcome of ER-phagy may vary depending on cancer type and microenvironmental context.

4.2 Ca^{2+} Signaling and Apoptosis

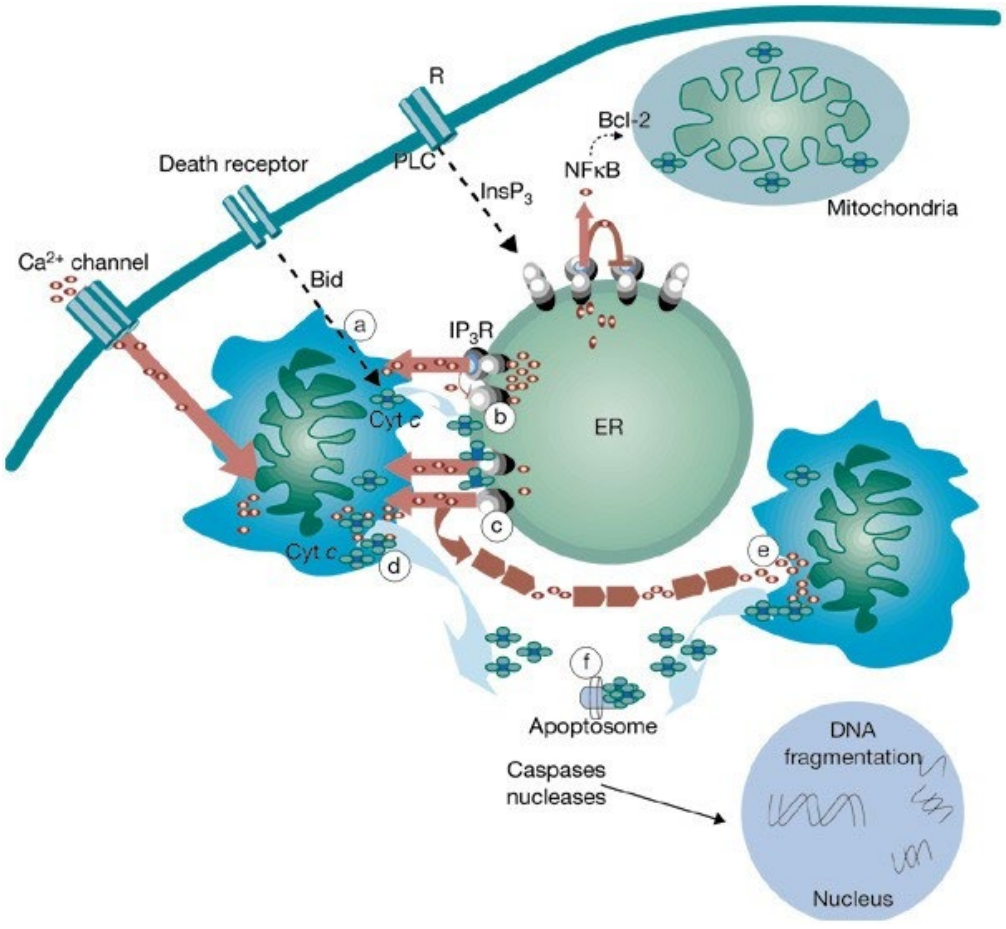

Fig. 4 Ca^{2+} released from the ER synchronizes the mass exodus of cytochrome *c* from the mitochondria, a phenomenon that coordinates apoptosis. Mattson et al. 2003.

Ca^{2+} signaling plays a central role in the regulation of apoptosis, acting as a crucial second messenger that orchestrates both pro-survival and pro-death pathways. Sustained or excessive cytosolic Ca^{2+} elevations, often due to release from the ER via inositol 1,4,5-trisphosphate receptors (IP3Rs), can lead to mitochondrial Ca^{2+} overload, activation of caspases, and induction of apoptosis (42). Conversely, tightly regulated Ca^{2+} fluxes are essential for mitochondrial metabolism and cell survival. In cancer cells, these pathways are frequently dysregulated: oncogenic mutations often reduce ER-to-mitochondria Ca^{2+} transfer, thereby avoiding mitochondrial permeability transition and apoptotic signaling (43). Proteins such as Bcl-2 and Mcl-1 can inhibit IP3R-mediated Ca^{2+} release, contributing to apoptotic resistance. Furthermore, altered expression of Ca^{2+} pumps (e.g., SERCA) and channels (e.g., MCU, RyR) has been observed in colorectal and other cancers, supporting the notion that Ca^{2+} homeostasis is reprogrammed to sustain tumor growth and therapy resistance (44). Understanding the interplay between ER-phagy, Ca^{2+} dynamics, and apoptotic escape may provide novel therapeutic angles to selectively target tumor cell vulnerability.

4.3 ER-phagy and Apoptosis: A Delicate Balance

Autophagy and apoptosis are tightly interconnected processes. ER-phagy, by relieving ER stress and removing pro-apoptotic signals (e.g., CHOP, caspase-12), can act as a survival mechanism (19). However, persistent ER stress or excessive ER fragmentation can trigger apoptotic pathways, especially through Ca^{2+}-dependent mechanisms and the activation of UPR effectors like PERK, ATF4, and ATF6 (45). In CRC, the interplay between ER-phagy and apoptosis is complex. On one hand, moderate ER-phagy may allow cancer cells to adapt to chemotherapeutic stress or nutrient deprivation. On the other, ER-phagy inhibition can lead to unresolved ER stress and promote apoptosis, particularly in tumors with intact TP53 (46).

4.4 Future Perspectives

As our understanding of ER-phagy and its intricate crosstalk with Ca^{2+} signaling and apoptosis deepens, FAM134B emerges as a pivotal regulator of cellular adaptation under stress conditions. In CRC, where ER stress and metabolic reprogramming are hallmarks of tumor progression, dissecting the functional role of FAM134B may

uncover novel vulnerabilities. Future studies should aim to elucidate the isoform-specific roles of FAM134B, its regulation by post-translational modifications, and its potential as a biomarker of ER-phagic activity. Furthermore, the development of therapeutic strategies that modulate FAM134B-mediated ER-phagy, either by enhancing it to promote cell death or inhibiting it to sensitize tumors to ER stress, represents a promising frontier in precision oncology.

Aim of the Thesis

The primary aim of this thesis is to elucidate the role of the ER-phagy receptor FAM134B in CRC cells, with a particular focus on its potential involvement in regulating intracellular Ca^{2+} signaling. Autophagy has a dual role in tumor suppression and adaptation, while ER-phagy is important in maintaining ER homeostasis. This study explores whether dysregulation of FAM134B-mediated ER-phagy contributes to the altered stress response, apoptotic resistance, and metabolic adaptation in CRC.

To this end, the thesis will:

- Explore whether modulation of FAM134B affects cellular responses to ER stress and cytotoxic treatments, thus identifying potential therapeutic vulnerabilities.
- Investigate the interplay between ER-phagy, Ca^{2+} fluxes, and mitochondria-ER contact sites (MAMs), with a focus on how FAM134B might influence cell survival and apoptosis in CRC models.

Ultimately, this work seeks to contribute to a deeper understanding of how selective autophagy pathways and FAM134B could be harnessed or targeted to improve cancer treatment strategies.

Methods

Cell culture

CCD 841-CoN, CaCo-2, SW480, SW48, HCT116 and HEK293T were purchased from ATCC. All cell lines were regularly tested for the presence of mycoplasma using LookOut Mycoplasma PCR Detection Kit (Sigma-Aldrich). The human colon epithelial cell line CCD 841-CoN was maintained in Minimum Essential Medium (MEM) supplemented with 10 % fetal bovine serum (FBS), 1 % Penicillin–Streptomycin, and 1 % non-essential amino acids (NEAA). CaCo-2 cells were cultured in Dulbecco's Modified Eagle Medium (DMEM) supplemented with 20 % FBS and 1 % Penicillin–Streptomycin. SW480 and SW48 cells were maintained in DMEM containing 10 % FBS and 1 % Penicillin–Streptomycin. HCT116 cells were cultured in Roswell Park Memorial Institute (RPMI) medium supplemented with 10 % FBS and 1 % Penicillin–Streptomycin. CRC inducible cells were treated with 1µg/ml of doxycycline to induce FAM134B expression and with 200ng/ml bafilomycin A1 to block autophagy. Stable CRC cell lines were generated using lentiviral virus infections. Lentiviruses were generated by co-transfecting in HEK293T cells with the pLTD vector, pPAX2 packaging plasmid, and pMD2.G envelope plasmid. Viral supernatant was harvested after 48 h and filtered through a 0.45-µm filter. CRC cells were incubated in six-well plates with 800 µl of viral supernatant and after 48h, the medium was replaced with antibiotic-containing medium.

Cell proliferation assay

Cell growth was monitored using the IncuCyte live-cell imaging system (Sartorius). Cells were seeded in 384-well plates with six technical replicates and three independent biological replicates for each condition. Seeding densities were optimized for each cell line according to their growth characteristics and culture medium, ensuring an initial confluence of approximately 20 % in all cases. Plates were then placed in the IncuCyte incubator, and brightfield images were acquired every hour over a period of 3 days to monitor cell proliferation in real time. The acquired images were subsequently analyzed using the IncuCyte analysis software to determine cell confluence over time.

Thapsigargin (TG) Dose-Response assay

For the dose-response experiment, cells were seeded in 384-well plates one day before treatment. The following day, cells were treated with increasing concentrations of TG using an Echo acoustic liquid handler (Labcyte), which allows the precise dispensing of nanoliter volumes. After treatment, plates were placed in the IncuCyte live-cell imaging system, and brightfield images were acquired every hour for a total duration of 72 hours. Image analysis was carried out using the IncuCyte analysis software to measure cell confluence over time for each well, allowing the assessment of cell growth in response to different TG concentrations.

Immunoblotting

Cells were harvested by removing the culture medium and washed with PBS 1X. Cells were lysed in ice-cold lysis buffer (150mM NaCl, 50mMTris-HCl pH 7.5, 1%Nonidet P-40 (NP-40)) supplemented with protease and phosphatase inhibitors and N-Ethylmaleimide (NEM)1mM. Insoluble cell components were separated at 15,500 × g for 20 min at 4°C. Protein denaturation was performed in Laemmli buffer at 95°C for 10min. Protein lysates were solved in SDS-PAGE gels and transferred to nitrocellulose or PVDF membrane. Membranes were saturated in TBS 0.1% Tween (Tris-buffered saline containing 0.1 % Tween-20) containing 5% low-fat milk and incubated overnight at 4 °C with the specific primary antibody (reported in Reagents and Tools). Secondary antibodies were diluted in 5 % low-fat milk prepared in TBS 0,1 % Tween and incubated with the membranes at room temperature.

Immunoprecipitation

Stable CRC cell lines were induced with doxycycline (1µg/ml) for 6 hours and harvested in 50 mM Tris/HCl (pH 8.0), 120mM NaCl, 1% NP40, complete protease and phosphatase inhibitors and N-Ethylmaleimide (NEM). Lysates were cleared by centrifugation at 10,000×g for 20 min and incubated for 1 h with monoclonal anti-GFP-agarose. Beads were then washed three times in wash buffer: 10 mM Tris/Cl pH 7.5, 150mM NaCl, 0.05% NP-40, 0.5 mM EDTA, resuspended in Laemmli buffer and boiled at 95°C. Supernatants were loaded on SDS-PAGE, and western blots were performed using the indicated antibodies.

Quantitative real-time PCR (qRT-PCR)

Total RNA extraction was performed using the RNeasy Mini Kit and the concentration and purity of RNA were measured using a spectrophotometer at 260/280nm. First-strand cDNA for qRT–PCR was generated using QuantiTect Reverse Transcription Kit. The primers were designed using online primer design software and are shown in Reagents and Tools. GAPDH was used as a housekeeping gene, and the data normalization was performed according to the 2-ΔΔCt method. The qRT–PCR experiments were performed using SYBR Green I Mastermix (Roche) and a Lightcycler96 instrument following the manufacturer's instructions.

Autophagy and ER-phagy flux

CRC cells were infected with a retrovirus vector carrying GFPLC3B-RFP or a lentivirus vector carrying ssRFP-GFP-KDEL obtained from the pCW57-CMV-ssRFP-GFP-KDEL. Fluorescence of GFP and RFP, as well as cell confluence and differentiation status, were monitored over time using the IncuCyte S3 (Sartorius, Germany) in a 384-well format. Cells were seeded in proper media, supplemented with Fetal Bovine Serum (FBS) and penicillin/streptomycin and monitored for 72 hours. Screens in the two channels were taken every hour following the treatment with BafA1 and Torin. Autophagy and ER-phagy flux were observed through changes in the ratio of the total fluorescence intensity respectively of GFP/RFP and RFP/GFP. Each point represents the averaged ratio of data obtained from five or six individual wells (technical replicates) and experiments have been performed in three biological replicates with comparable results. For GFPLC3B-RFP construct, where the RFP is cleaved upon LC3B lipidation and not degraded into lysosome, we used the RFP as normalizer to have a cell number independent readout.

Fluorescence microscopy

CRC cells were plated on glass coverslips and fixed with 4% paraformaldehyde for 15 min. Cells were permeabilized for 5 minutes using PBS supplemented with 0.1 % saponin at room temperature and then blocked in PBS containing 10% fetal bovine serum (FBS) for an additional hour at room temperature. Cells were incubated overnight at 4 °C with primary antibody diluted in PBS with the same detergent used during permeabilization. Washes were performed in PBS with the same detergent used during permeabilization. Cells were incubated with secondary antibodies for 1 hour at

room temperature and then washed 3 times. Nuclei were stained with Hoechst 33342. The coverslips were mounted on slides with an aqueous mounting medium (Mowiol) and placed on a glass holder. Images were acquired with a Zeiss LSM800 or LSM900 laser scanning microscope (63× oil objective) controlled by the Zen blue software. The images were processed with Fiji (ImageJ; National Institute of Health (NIH)) software.

Antibodies used for Western Blot and Immunofluorescence staining

For Western Blot and Immunofluorescence, the following primary antibodies were used: anti-LC3B (Nanotools, Clone 5F10), anti-p62 (Cell Signaling Technology), anti-Vinculin (Sigma), anti-REEP5 (Proteintech), anti-GAPDH (Santa Cruz Biotechnology), anti-FAM134B (Sigma-Aldrich), anti-TOMM20 (GeneTex), anti-ATP2A2 (Cell Signaling) and anti-PARP (Cell Signaling).

The corresponding secondary antibodies used for Western blotting were horseradish peroxidase (HRP)-conjugated anti-mouse and anti-rabbit antibodies (Millipore).

For immunofluorescence experiments, fluorescently labeled secondary antibodies were employed: Alexa Fluor 555-conjugated anti-rabbit (Thermo Fisher Scientific), Alexa Fluor 647-conjugated anti-rat (Thermo Fisher Scientific), and Alexa Fluor 488-conjugated anti-mouse (Thermo Fisher Scientific).

Cloning procedures

cDNAs were cloned into lentiviral vectors using GATEWAY (ThermoFisherScientific) systems. The cDNAs were cloned into the pDONR223 vector using the BP Clonase Reaction Kit (Thermo Fisher Scientific) and further recombined, though the LR Clonase Reaction Kit (Thermo Fisher Scientific), into GATEWAY lentiviral destination vectors: pLTD-N-HA-PUROMYCIN lentiviral vector. We designed pLTD-N-HA-BLASTICIDIN lentiviral vectors that were generated by Vector Builder. Using the above lentiviral plasmid backbones, we enzymatically changed the tag from HA to RFP, V1 (nonfluorescent N-terminus of Venus, Met1-Gln157) and V2 (non-fluorescent C-terminus of Venus, Lys158-Lys238). V1 and V2 tags were amplified by PCR fromV1 andV2-pcDNA3.1 (from Prof. Ivan Dikic).

Generation of CRC FAM134B knockout cells

The FAM134B knockout CRC cell lines were generated using a lentiviral CRISPR–Cas9 system. sgRNAs, were designed using the Broad Institute genetic perturbation platform (https://portals.broadinstitute.org/gpp/public/analysistools/sgrna-design). Oligonucleotides were cloned into the lentiviral vector pKLV2.2-h7SKgRNA5(SapI)-hU6gRNA5(BbsI)-EF1aCas9-FLAG-P2A-BSDR, kindly provided by Dr. Koraljka Husnjak and Prof. Ivan Dikic. Oligonucleotides for the gRNAs were annealed and phosphorylated using T4 polynucleotides kinase. To clone the first gRNA, the vector was digested with BsmBI enzyme, while to clone the second gRNA, the vector was digested with SapI. The ligase reaction was achieved using the T4 ligase. Following the lentiviral transduction, cells were selected with 20 μg/ml Blasticidin for 2 weeks.

Mass spectrometry

All the experiments were performed in a labeling-free setting. Proteins were precipitated in acetone and then reduced and alkylated in a solution of 6M Guanidine-HCl, 5mM TCEP, and 20 mM chloroacetamide. Peptides were obtained by digesting proteins with LysC (WAKO) for 3h at 37°C and with sequencing-grade endopeptidase Trypsin (Promega) overnight at 37 °C. Collected peptide mixtures were concentrated and desalted using the Stop and Go Extraction (STAGE) technique. Peptides were obtained by Trypsin/LysC digestion and cleaned up using SDB-RPS stage tips. Instruments for LC MS/MS analysis consisted of a NanoLC 1200 coupled via a nano-electrospray ionization source to the quadrupole-based Q Exactive HF benchtop mass spectrometer. Peptides were separated based on their hydrophobicity using an analytical column (75 μm) in-house packed with C18-AQ resin (1.9 μm particles). The separation was performed with a linear gradient from 7% to 32% solvent B over 45 min, followed by 32% to 45% B in 5 min, 45% to 95% B in 3 min, and re-equilibration from 95% to 5% B in 5 min, at a flow rate of 300 nL/min.

MS data were acquired in DIA (Data-Independent Acquisition) mode using 32 variable isolation windows covering a mass range of 300–1650 m/z. The resolution was set to 60,000 for MS1 and 30,000 for MS2. The AGC target was 3×10^6 for both MS1 and MS2, with maximum injection times of 60 ms and 54 ms, respectively. Normalized collision energies (NCE) were set to 25%, 27.5%, and 30%.

BiCAP interactome analysis

We generated stable and inducible (via doxycycline) CRC cells expressing the lentiviral plasmids carrying a Split GFP tag: V1-FAM134B1/V2-FAM134B1. We induced FAM134B expression for 6 h and then lysed samples (150mM NaCl, 50mM Tris-HCl pH 7.5, 1% Nonidet P-40 supplemented with protease and phosphatase inhibitors and N-Ethylmaleimide (NEM) 1mM). If the two V1 and V2 tags are in proximity they will associate to re-establish the full GFP molecule. We incubated 1mg of sample lysate with GFP-trap beads (Chromoteck) for 1h on a rotating wheel at 4°C. Beads were then washed three times with cold lysis buffer and once in PBS before on-bead trypsin digestion. Beads were then incubated with 25 µl SDC buffer (2% sodium deoxycholate, 1mM TCEP, 4mM chloroacetamide and 50 mM Tris-HCl pH 8.5) and heated at 60°C for 30 min. We then digested samples with trypsin overnight at 37 °C (500ng trypsin and 500ng LysC in 25µl 50mM Tris-HCl pH 8.5). Digestion was blocked with 150 ml of 1%TFA in isopropanol. Peptides were purified using C18 stage tips (Empore). We washed peptides with 1% TFA in isopropanol and with 0.2% TFA in water. Peptides were eluted with 80% acetonitrile plus 1.25% ammonia. Peptides were dried and processed for the LC-MS/MS.

Caspase activation assay

Apoptotic cell death was monitored using two complementary approaches: live-cell imaging with the IncuCyte system and end-point quantification with the Caspase-Glo 3/7 Assay (Promega).

For real-time analysis, cells were seeded in 384-well plates at densities optimized for each cell line to achieve an initial confluence of approximately 20%. The following day, cells were treated with 10 nM TG in combination with the IncuCyte Caspase-3/7 Red Reagent for Apoptosis (Sartorius), following the manufacturer's instructions. Plates were then placed in the IncuCyte incubator, and images were acquired every hour for 72 hours using both brightfield and red fluorescence channels. Brightfield imaging was used to monitor cell confluence over time, while the red fluorescence signal detected caspase-3/7 activation as a dynamic marker of apoptosis. Image analysis was performed using the IncuCyte Analysis Software, quantifying both cell growth and apoptotic activity in each well over time.

In parallel, apoptosis was also evaluated using the Caspase-Glo 3/7 Assay System (Promega), according to the manufacturer's protocol. Cells were seeded in 96-well

plates and treated with 10 nM TG for 48 hours. After incubation, an equal volume of Caspase-Glo 3/7 reagent was added to each well, and the luminescent signal, proportional to caspase-3/7 activity, was measured using a GloMax Discover Microplate Reader (Promega). This end-point assay served to validate and complement the kinetic analysis obtained with IncuCyte, ensuring quantitative assessment of apoptotic induction across all experimental conditions.

Tunel assay

Apoptotic cell death was assessed using the Click-iT TUNEL Alexa Fluor 647 Imaging Assay (Thermo Fisher Scientific), following the manufacturer's instructions. Cells were seeded on poly-L-lysine–coated 96-well plates and allowed to adhere for 24 h. Cells were then treated with 10 nM TG for 48 h and after treatment, cells were fixed and permeabilized according to the kit protocol. DNA strand breaks were labeled with modified dUTP using terminal deoxynucleotidyl transferase (TdT), followed by a Click-iT reaction to incorporate Alexa Fluor 647 azide. Nuclei were counterstained with DAPI. Plates were subsequently analyzed and imaged using the High Content Screening (HCS) Facility at TIGEM. Image acquisition and quantification were performed using automated high-content imaging systems to evaluate the percentage of TUNEL-positive nuclei.

Intracellular Ca^{2+} imaging assay

SW480 cells were cultured in µ-Plate96 microplates (Ibidi) precoating treated at subconfluent condition. Cells were washed 2 times with PBS (120 µl/wash) and then incubated (1h, 37°C) with Fluo-4 AM probe (F23917, Thermo Fisher Scientific) 5 µM in PBS containing 10 mM glucose, 0.5 mM sulfinpyrazone and 1% fetal bovine serum. After, cells were washed 2 times with PBS-glucose-sulfinpyrazone solution (120 µl/wash) and then 100 µl/well of the same buffer was added to allow dye de-esterification. To study the mechanism of SERCA protein and the inhibition of extracellular Ca^{2+}, the same experiment was conducted using Ca^{2+}-free PBS. Each well was assayed individually with a system consisting of an inverted Olympus microscope equipped with a 40x oil immersion objective and a 530 nm emission filter, a high speed wavelength switcher (Lambda DG4, Sutter Instrument Co., Novato, CA, USA) carrying a 490 nm excitation filter, a Prime cmos camera (Photometrics, Tucson, AZ, USA), and the MetaFluor acquisition software (Molecular Devices, Sunnyvale, CA,

USA). Each well was assay individually. Time-lapse Fluo-4-fluorescence (500 nm excitation, 535 nm emission) microscopy experiments were carried out using the following conditions: 50 ms exposure time, 1s interval, and 3 min total duration. Ten seconds after the start of recording, cytosolic Ca^{2+} mobilization was induced by acute stimulation with 100 µl of 1 µM TG final concentration. Analysis was performed with MetaFluor software, by measuring Fluo-4 fluorescence in manually selected single cell regions of interest (ROI). After background subtraction, the fluorescence trace for each ROI was normalized to the initial value. Eight cells were selected in each field to generate an average trace.

Mitochondrial Ca^{2+} assay

Mitochondrial Ca^{2+} dynamics were monitored using the fluorescent probe Rhod-2 AM (R1245MP Thermo Fisher Scientific). SW480 cells were cultured in µ-Plate96 microplates (Ibidi) pre-coated at subconfluent condition. On the day of the experiment, cells were incubated with Rhod-2 AM (2 µM) in DMEM containing 10 % FBS and 1 % Penicillin–Streptomycin for 45 minutes at 37 °C, followed by two washes with PBS containing 2mM Ca^{2+} and 10mM Glucose, and then 100 µl/well of the same buffer were added to allow allow complete cleavage of AM esters and mitochondrial accumulation of the dye. Live-cell fluorescence measurements were performed using a fluorescence microscope equipped with 40X oil immersion objective (Olympus, Segrate, Italy), a high speed wavelength switcher (Lambda DG4, Sutter Instrument Co., Novato, CA, USA), a Prime cmos camera (Photometrics, Tucson, AZ, USA), and the Meta-Morph software (Molecular Devices, Sunnyvale, CA, USA). Each well was assayed individually. Time-lapse Rhod-2-fluorescence (552 nm excitation, 552/581 nm emission) experiments were carried out with the following conditions: 50ms exposure time, 5s interval, and 4 min total duration. After 5 s, 100 µl of 1 µM TG final concentration was added, and fluorescence was recorded over time. Changes in cell fluorescence were quantified with MetaMorph software by measuring Rhod-2 fluorescence in manually selected regions of interest (ROI). After background subtraction, the fluorescence trace for each ROI was normalized to the initial value. Eight cells were selected in each field to generate an average trace.

Proximity Ligation Assay (PLA)

Protein–protein interactions were analyzed using the Duolink In Situ Red kit (Sigma–Aldrich) according to the manufacturer's instructions. SW480 cells were cultured on coverslips and fixed with 4 % paraformaldehyde (PFA), followed by permeabilization for 10 minutes with PBS supplemented with 0.1 % saponin. After permeabilization, samples were incubated with Duolink blocking solution to prevent non-specific antibody binding. Cells were then incubated overnight at 4 °C with primary antibodies against IP3R (inositol 1,4,5-trisphosphate receptor) and VDAC1 (voltage-dependent anion channel 1), raised in mouse and rabbit, allowing the use of species-specific PLA probes. The following day, the PLA probes (PLUS and MINUS) were applied, followed by ligation and amplification steps to generate fluorescent signals indicating protein proximity. The Duolink In Situ Red detection reagents were used for signal development. Nuclei were counterstained with DAPI, and coverslips were mounted and imaged using a Zeiss LSM 900 confocal microscope. Image analysis was performed using Fiji/ImageJ. PLA fluorescent puncta were quantified by applying a particle analysis threshold with a size range of 0.2 μm² to 0.5 μm² and a circularity of 0.5–1.0, ensuring consistent detection parameters across all samples. The number of PLA dots was then normalized to the number of nuclei in each field. For each experimental condition, approximately 100 cells were analyzed to ensure statistical robustness.

Mitochondrial Stress Test

Mitochondrial respiration was assessed using the Seahorse XF HS Mini Analyzer (Agilent) and the Mito Stress Test assay according to the manufacturer's instructions. SW480 cells were seeded at a density of 20,000 cells per well in XF cell culture microplates and cultured overnight in their standard growth medium. On the day of the experiment, cells were washed once with Seahorse XF DMEM Base Medium supplemented with 10 mM glucose, 2 mM glutamine, and 1 mM pyruvate (pH 7.4), and then incubated in the same assay medium for 1 hour at 37 °C in a non-CO_2 incubator to allow medium equilibration. The assay was performed by sequential injections of the following mitochondrial modulators: oligomycin (1 μM) to inhibit ATP synthase, FCCP (1 μM) to uncouple the mitochondrial membrane and reveal maximal respiration, and rotenone/antimycin A (1 μM each) to inhibit complexes I and III, respectively, allowing the determination of non-mitochondrial respiration. At the

end of the experiment, cell number was determined (using DAPI staining) through Apotome microscope, and results were normalized to cell number to account for potential variations in seeding density. For each well, the absolute number of cells was entered in the Agilent Wave software and a scaling factor of 10^4 was applied, in accordance with the manufacturer's guidelines. Normalized OCR values are expressed as pmol O_2/min/10^4 cells. This approach corrects for well-to-well variations in seeding density and allows direct comparison between experimental conditions (Agilent Technologies, XF Data Normalization Technical Guidelines, 2018).

Data analysis

All experiments were performed in at least three independent biological replicates. Data are presented as mean±s.e.m or s.d. Statistical analysis between two experimental groups was performed using a parametric two-tailed Student's t test or ANOVA. For immunostaining quantifications, cells were analyzed for each experimental condition in each replicate. To analyze PLA dots, 100 cells per condition were counted and subsequently measured using the Analyze particle function of the Fiji software. For autophagy flux experiments, data obtained from one scan containing >1000 cells of three or four different wells with indicated treatment were analyzed.

MS data elaboration

RAW files were analyzed using Spectronaut (v. 18, 19, 20), ran in library-free search (directDIA). To assess protein identification and quantification, default parameters were used: precursor ion mass tolerance: dynamic; Orbitrap fragment ion mass tolerance: dynamic (Spectronaut); fixed modifications: cysteine carbamidomethylation; variable modifications: methionine oxidation, protein N-terminus acetylation, enzyme: trypsin, Lys-C; the number of allowed missed cleavage sites: 2; minimum peptide length: seven amino acid residues. The DIA spectra were probed against UniProt Homo Sapiens (UP000005640_2025) FASTA database. MS data were filtered at 1% FDR on the protein level and exported, followed by analysis with different software packages (Excel, Rstudio, SRplot). Specifically, statistical analyses for quantitative evaluation were performed using Perseus software (1.6.2.3), the subtraction of contaminants, reverse entries as well as the identification by a modified peptide only, were applied as the first filter. The LFQ ratios were logarithmized, grouped, and filtered for min. valid number (min. 3 or 2 in at least one group). Missing values were replaced by random numbers that are drawn from a

normal distribution. For the comparison among the different conditions in terms of protein abundance level, Anova and Student's t test were used. For each test, the level of significance was set equal to 0.05. Proteins with at least $\log_2$ onefold changes were considered differentially regulated. A Gene Ontology (GO) and KEGG enrichment analysis was carried out on dysregulated proteins.

Results

1. Characterization of FAM134B expression and ER architecture across Colorectal cancer cell lines (CRC)

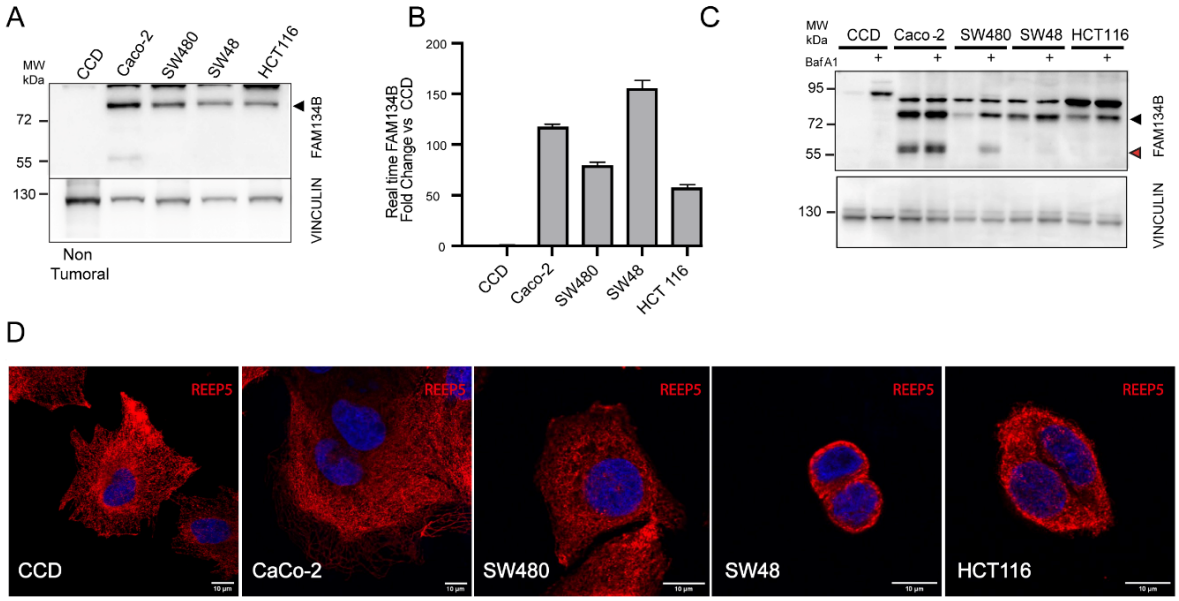

Figure 1. Characterization of FAM134B expression and ER morphology in CRC cell lines. **(A)** Western blot analysis of basal FAM134B protein levels in the non-tumoral epithelial CCD cells and CRC-derived cell lines (Caco-2, SW480, SW48, HCT116). Vinculin was used as a loading control. **(B)** Real-time PCR analysis of FAM134B mRNA expression in the same panel. Data are presented as fold change relative to CCD. **(C)** Western blot analysis of FAM134B levels (black arrow) following treatment with Bafilomycin A1 (BafA1). Accumulation of FAM134B in SW480, SW48 and HCT116 cells indicates active lysosomal turnover, while the weaker response in Caco-2 suggests lower degradation dynamics or a reduced ER-phagy flux. Red arrow indicates the short isoform of FAM134B. Vinculin was used as a loading control. **(D)** Immunofluorescence staining of the ER marker REEP5 (red) to visualize ER morphology in CCD and CRC cell lines. Nuclei are counterstained with DAPI (blue). Scale bar 10 µm.

To investigate the role of FAM134B in CRC, we selected a panel of human CRC cell lines displaying distinct morphological and molecular features. As a non-tumoral reference, we employed the CCD 841-CoN (CCD) cell line derived from normal colon epithelium. As CRC models, we included Caco-2 (differentiated, epithelial-like), SW480 (moderately differentiated adenocarcinoma), SW48 (poorly differentiated), and HCT116 (highly proliferative) cells. These models were used throughout this work to assess FAM134B expression, turnover, and potential involvement in ER-phagy and ER homeostasis.

We first examined FAM134B basal expression via Western Blot (Figure 1A). FAM134B was completely absent in non-tumoral CCD cells, while it was clearly detected in all CRC-derived lines, albeit at different protein levels. Among them, Caco-

2 displayed the highest basal protein level, followed by SW48 and SW480, whereas HCT116 showed comparatively lower expression.

To validate these results, at transcriptional level, we quantified FAM134B mRNA via real-time PCR (Figure 1B). Consistent with protein data, FAM134B transcripts were undetectable in CCD cells but markedly present in all CRC cell lines, with Caco-2 and SW48 showed the highest fold increase relative to the non-tumoral control.

Given that FAM134B acts as an ER-phagy receptor targeted for lysosomal degradation (22), we next assessed whether its turnover was affected by lysosomal inhibition. Treatment with Bafilomycin A1 (BafA1), which blocks autophagosome-lysosome fusion (47), led to a clear accumulation of FAM134B in SW480, SW48, and HCT116 cells, indicating ongoing lysosomal degradation under basal conditions (Figure 1C). Interestingly, despite their high basal levels, Caco-2 cells displayed only mild accumulation upon BafA1 treatment, suggesting distinct degradation kinetics, possibly reflecting a slower ER-phagy flux or stabilization of FAM134B. Of note, a shorter isoform of FAM134B was detected in both untreated and treated Caco-2 cells, and in treated SW480 cells.

To further explore whether these differences in FAM134B expression and turnover correlate with ER organization, we analyzed ER morphology by immunofluorescence staining of REEP5, a structural protein that shapes the ER network (48). As shown in Figure 1D, CCD cells displayed a relatively simple and diffuse ER network, characterized by thin tubules dispersed throughout the cytoplasm. Differently, Caco-2 cells showed an extensive, perinuclear ER network with densely packed and elongated tubules. SW480 and SW48 cells exhibited highly reticulated and interconnected ER structures, while HCT116 cells displayed a more compact ER, often forming dense perinuclear clusters consistent with enhanced metabolic or secretory activity. These morphological differences suggest that CRC cells undergo profound remodeling of the ER network, possibly reflecting adaptations in membrane dynamics, protein-folding capacity, and ER-phagy activity.

Collectively, these observations demonstrate that FAM134B is selectively expressed in CRC-derived models and undergoes constitutive lysosomal degradation in most of them. The distinct ER morphology and differential FAM134B turnover highlight a heterogeneous engagement of ER-phagy-related mechanisms across CRC cell lines, potentially reflecting differences in ER stress adaptation and proteostasis regulation.

2. Global proteomic profiling reveals ER-related pathways in CRC cell models

Following the characterization of FAM134B expression and ER morphology (Figure 1), we next sought to obtain a comprehensive overview of the molecular landscape of the same CRC cell lines. To this aim, we performed an unbiased, label-free quantitative proteomic analysis to compare the global protein expression profiles across all five cell lines.

Total protein extracts were processed and analyzed by LC–MS/MS, followed by bioinformatic processing for peptide identification and quantification (Figure 2A).

The Principal Component Analysis (PCA) revealed a clear segregation between the non-tumoral CCD cells and the CRC-derived lines, indicating distinct global proteomic signatures (Figure 2B). Among the cancer models, Caco-2 cells clustered separately from SW480, SW48, and HCT116, suggesting a unique proteomic identity possibly linked to their differentiated epithelial phenotype, conversely, SW480, SW48, and HCT116 displayed closer profiles. This spatial distribution highlights the intrinsic heterogeneity of CRC models even under basal conditions.

Consistently, hierarchical clustering confirmed two major branches separating non-tumoral from cancer-derived cells (Figure 2C). Within the CRC group, Caco-2 again clustered independently, further supporting its distinct proteomic landscape and reinforcing the trend observed in the PCA plot.

To identify the most significantly enriched biological pathways, we performed KEGG pathway analysis on the detected proteins (Figure 2D). Among the top ten categories, we found enrichment in pathways related to metabolism, ribosomal biogenesis, and protein processing in the ER. Notably, the latter term “Protein processing in ER” directly connects the proteomic data with our previous observations on ER organization and FAM134B dynamics, suggesting that ER homeostasis and quality control mechanisms are differentially regulated across CRC cell lines.

This enrichment prompted us to further investigate processes associated with ER maintenance and degradation, in particular autophagy and ER-phagy, as potential adaptive mechanisms contributing to tumor cell homeostasis (35).

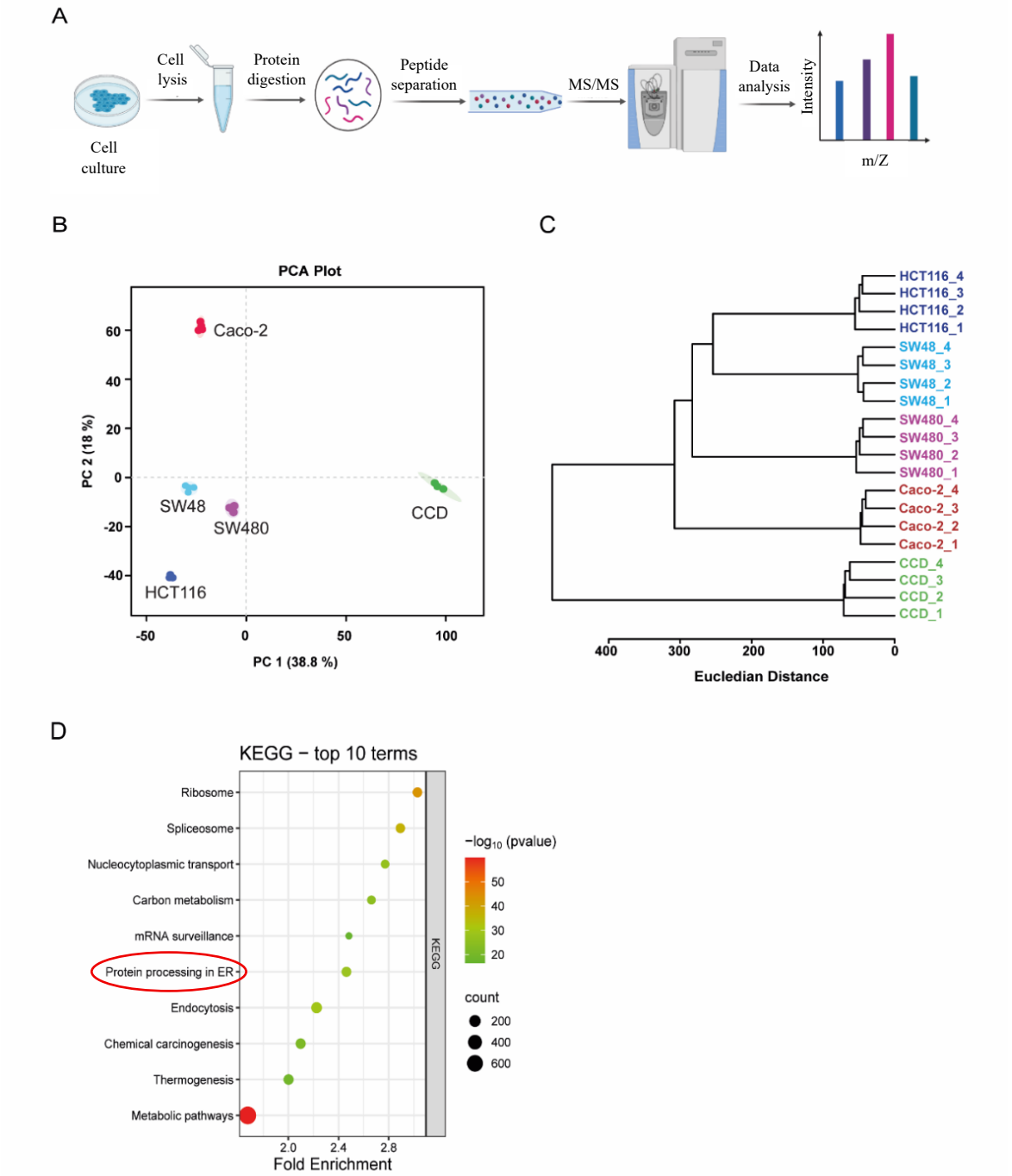

Figure 2. Full proteome analysis of CRC cell models. **(A)** Schematic workflow of the mass spectrometry-based proteomic approach. **(B)** Principal Component Analysis (PCA) showing the distribution of non-tumoral (CCD) and CRC cell lines based on global proteomic profiles. **(C)** Hierarchical clustering dendrogram confirming the separation between CRC cell lines and non-tumoral controls. **(D)** KEGG pathway enrichment analysis of detected proteins.

3. Autophagy and ER-phagy fluxes in CRC

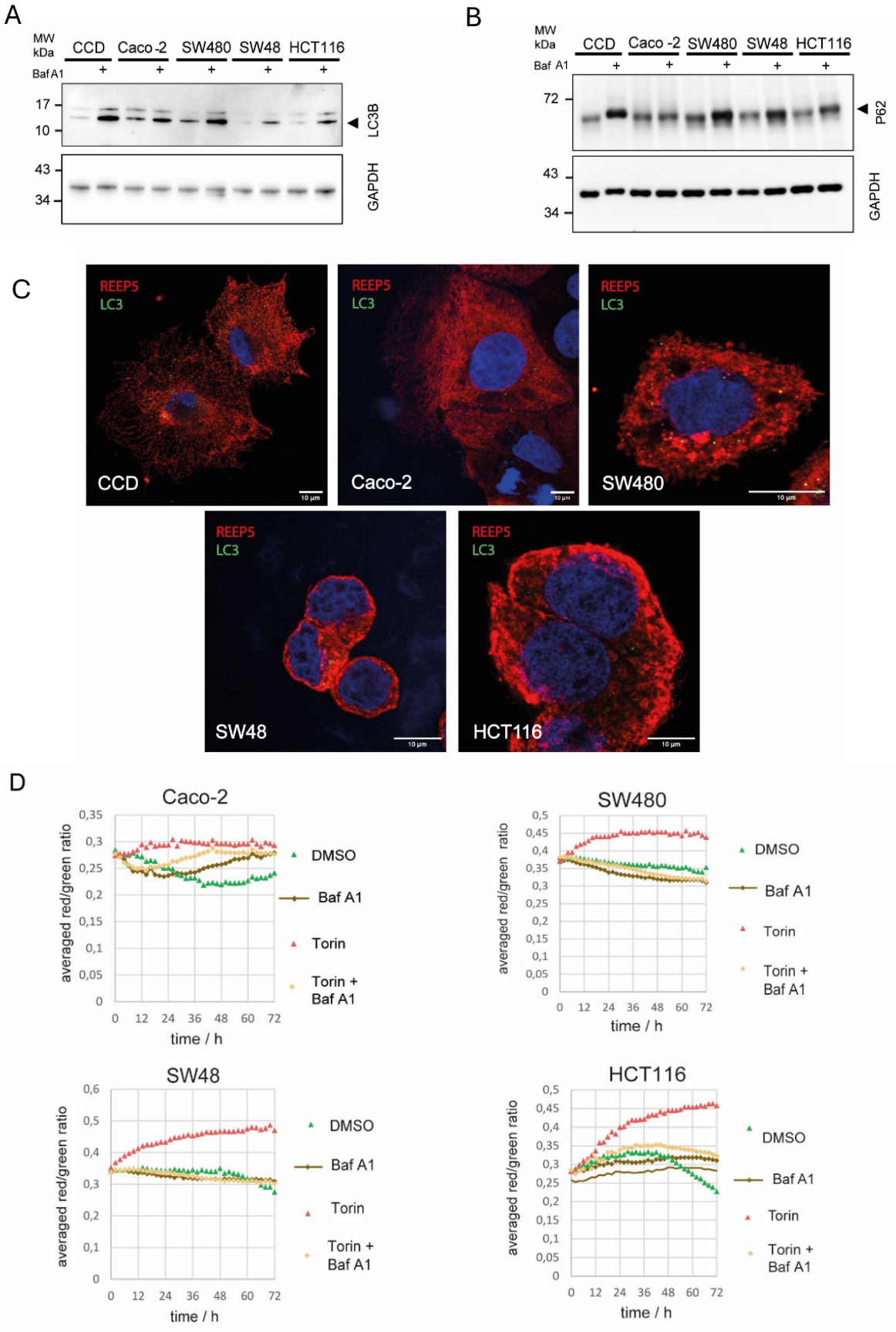

Fig**ure 3. Evaluation of autophagy and ER-phagy flux in CRC and non-tumoral cell models**. **(A,B)** Western blot analysis of LC3 and p62 in CCD, Caco-2, SW480, SW48, and HCT116 cells treated or not with Bafilomycin A1 (BafA1). GAPDH serves as a loading control. **(C)** Immunofluorescence imaging of REEP5 (ER marker, red) and LC3 (green). Nuclei are stained with DAPI (blue). Scale bar 10 µm. **(D)** ER-phagy flux monitored via Incucyte live-cell imaging of RFP-GFP-KDEL-expressing cells treated with DMSO, BafA1, Torin, or Torin plus BafA1. The red/green ratio increases in SW480, SW48 and HCT116, reflecting higher ER-phagy activity compared with Caco-2.

Building upon the global proteomic profiling (Figure 2), which revealed alterations in pathways related to protein processing in the ER, we next sought to assess whether these molecular differences translated into functional changes in autophagy and ER-phagy.

Given the close relationship between ER homeostasis, proteostasis, and degradative pathways (49), we examined both the general autophagic flux and the ER-specific turnover across the same panel of CRC cell models.

We monitored LC3 and p62/SQSTM1 levels upon lysosomal inhibition with Bafilomycin A1 (BafA1), which blocks autophagosome-lysosome fusion (47). LC3 is conjugated to phosphatidylethanolamine to form LC3-II, a hallmark of autophagosome formation, whose accumulation in the presence of BafA1 reflects ongoing autophagy (49). CCD, Caco-2 and SW480 cells displayed marked LC3-II accumulation upon BafA1 treatment, indicating a strong basal autophagic flux. Differently, SW48 and HCT116 cells showed only a moderate increase, suggesting limited autophagic activity under basal conditions (Figure 3A).

We next examined p62/SQSTM1, an autophagic adaptor that mediates cargo recruitment and is itself degraded during the autophagy process (50). CCD, SW480, SW48, and HCT116 exhibited a clear p62 accumulation after BafA1 treatment, while Caco-2 remained largely unresponsive, indicating that autophagic turnover is reduced in Caco-2 compared with the other models (Figure 3B).

To visualize the cellular distribution of autophagic structures in relation to ER organization, we performed immunofluorescence staining for REEP5 (ER-shaping protein) and LC3 (autophagosome marker). CCD and Caco-2 cells showed an extended, reticular ER structure with sparse LC3-positive puncta. Differently, SW480, SW48, and HCT116 cells exhibited a more compact and fragmented ER architecture, accompanied by LC3 puncta in proximity to ER membranes (Figure 3C).

To specifically monitor ER-phagy flux, we used live-cell imaging of ssRFP-GFP-KDEL stably expressing cells, which enables quantitative assessment of ER

degradation in lysosomes (Figure 3D). The tandem ssRFP-GFP-KDEL construct labels the ER lumen with both pH-sensitive GFP and acid-resistant RFP. Upon lysosomal delivery, GFP fluorescence is quenched while RFP persists, allowing quantification of ER-phagy flux through the red/green fluorescence ratio (51). Cells were treated with DMSO, BafA1, Torin1 (mTORC1 inhibitor), or Torin1 plus BafA1. Since FAM134B is not expressed in CCD cells, the analysis was restricted to Caco-2, SW480, SW48, and HCT116.

In Caco-2, the red/green ratio increased only modestly upon Torin1 treatment, suggesting limited activation of the ER-phagy machinery and confirming previous results. Differently, SW480, SW48, and HCT116 showed a robust increase in the ratio over time (Torin1, red line) confirming active and dynamic ER-phagy flux in these models. These data indicate that autophagy and ER-phagy are differentially regulated across CRC cell lines, with Caco-2 exhibiting lower flux and the other cancer models displaying enhanced degradative capacity and ER remodeling potential. Given that FAM134B acts as a key ER-phagy receptor, these functional differences may arise from context-dependent modulation of its activity or interactions.

To address this hypothesis, we next performed a FAM134B interactome analysis by immunoprecipitation followed by mass spectrometry (IP–MS). This approach aimed to identify potential FAM134B-binding partners in each cell line and determine whether the composition of its interactome changes in association with the differential ER-phagy activity observed across models.

4. FAM134B interactome reveals conserved SERCA2 binding in CRC cells

Knowing that autophagy and ER-phagy differ functionally among CRC cell models (Figure 3), we next investigated whether these variations could reflect distinct FAM134B interaction networks. Since FAM134B functions as an ER-phagy receptor that couples ER membranes to the autophagic machinery (12), we reasoned that differences in its protein partners might underlie the heterogeneous ER-phagy activity observed across the cell lines. To identify the molecular partners of FAM134B in CRC cell lines, we employed a BiCAP (bimolecular complementation affinity purification) approach. In this system, two non-fluorescent GFP fragments are fused to FAM134B. Upon oligomerization and clustering of FAM134B, the two GFP halves reconstitute a functional GFP molecule, enabling the selective immunoprecipitation (IP) of FAM134B-containing complexes using an anti-GFP antibody. This strategy allows the

isolation of FAM134B interactors under more physiological conditions (FAM134B forms clusters when active) (52), thus preserving both stable and transient associations. (A) Proteomic analyses of the immunoprecipitated fractions revealed a reproducible enrichment of FAM134B-associated proteins across different CRC cancer cell lines. The volcano plots display significantly enriched proteins ($p < 0.05$, fold change > 2) in each condition, revealing both shared and cell line–specific interactors. Among them, several proteins were related to autophagy and ER-phagy, Ca^{2+} homeostasis and ion binding, mitochondrial organization, and apoptotic signaling. Of note, ATP2A2 (SERCA2), the sarco/endoplasmic reticulum Ca^{2+} ATPase responsible for pumping cytosolic Ca^{2+} into the ER lumen, emerged as a consistent and robust FAM134B interactor across all cell lines.

(B) Functional clustering of the interactome datasets revealed that the majority of FAM134B partners were involved in:

- Ion binding and Ca^{2+} signaling, including Ca^{2+} transporters and regulators of ER–mitochondria Ca^{2+} exchange;
- Autophagy and ER-phagy, comprising selective autophagy receptors and autophagic core components;
- Mitochondrial processes, supporting a possible crosstalk between FAM134B and mitochondrial dynamics;
- ER structure and stress response, involving resident chaperones and ER-shaping proteins;
- Apoptotic regulation, including key players in ER-stress induced cell death.

The recurrent identification of ATP2A2/SERCA2 among its interactors points to a functional coupling between FAM134B and ER Ca^{2+} regulation; potentially linking the degradation of ER subdomains to Ca^{2+} dynamics and organelle communication.

(C) To biochemically validate this interaction, co-immunoprecipitation (Co-IP) experiments were carried out in SW480 cells expressing FAM134B under a doxycycline-inducible promoter. As shown in the immunoblots, FAM134B expression was robustly induced upon doxycycline treatment (plus DOX), while it was absent in untreated cells (minus DOX). Notably, ATP2A2 was co-immunoprecipitated only in the plus DOX condition, demonstrating that its association is dependent on FAM134B

expression. The absence of ATP2A2 signal in the minus DOX IP confirms the specificity of the interaction, excluding non-specific binding to the GFP tag or the beads. Together, these results provide biochemical confirmation that FAM134B physically associates with ATP2A2, reinforcing the proteomic findings obtained by MS.

These findings suggest that FAM134B may contribute to Ca^{2+} handling at the ER, potentially coupling ER-phagy activity with Ca^{2+} flux regulation and ER–mitochondria Ca^{2+} buffering.

Among the analyzed models, SW480 cells were chosen for subsequent experiments due to their detectable FAM134B expression, measurable ER-phagy activity, and validated interaction with ATP2A2/SERCA2. Furthermore, SW480 cells, derived from a primary colorectal adenocarcinoma (53), are widely used as a representative model of CRC; they harbor characteristic mutations in *APC*, *KRAS*, and *TP53* (54–56), which reflect key molecular alterations occurring during tumor development (57). For this reason, they are considered a reliable and well-characterized system for functional studies in CRC research. The rationale for this choice will be further explained in the following sections.

Although FAM134B shared some common interactors across CRC lines, the composition of its interactome varied, indicating context-dependent remodeling. To assess the functional consequences of FAM134B loss, we next generated FAM134B knockout (KO) SW480 cells, which were used for subsequent phenotypic and functional analyses.

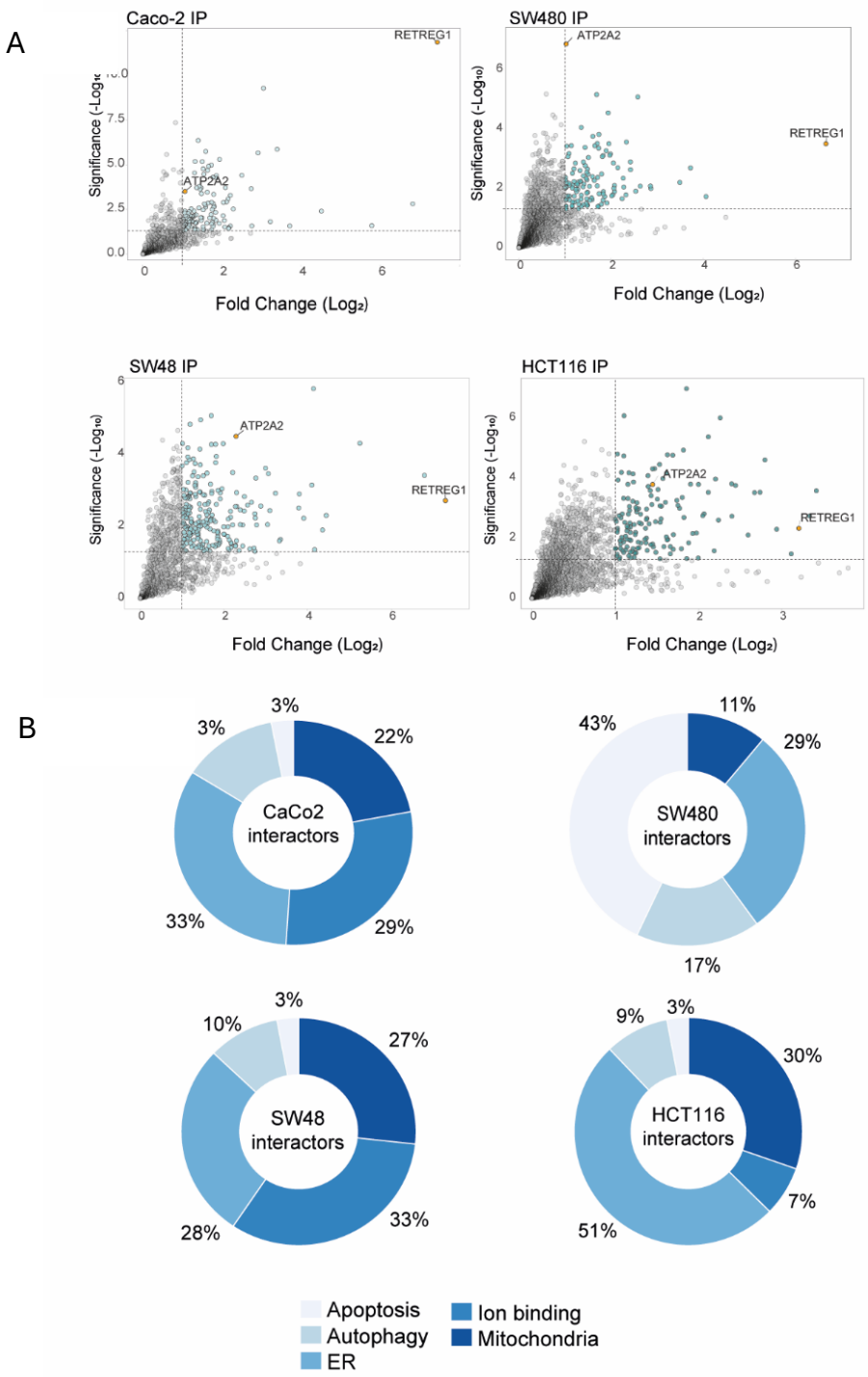

Figure 4. Interactome analysis of FAM134B in CRC cancer cell lines

(A) BiCAP-based GFP immunoprecipitation followed by proteomic analysis identifies FAM134B-associated protein interactors in distinct CRC cell lines. Volcano plots display significantly enriched interactors. **(B)** Functional categorization of FAM134B interactors. **(C)** Biochemical validation of the FAM134B–ATP2A2 interaction in SW480 cells. Co-IP confirms that ATP2A2 binds specifically to FAM134B upon doxycycline induction (plus DOX), while no signal is detected in uninduced cells (minus DOX).

5. Altered ER morphology and sensitivity to SERCA inhibition in SW480 FAM134B knockout cells

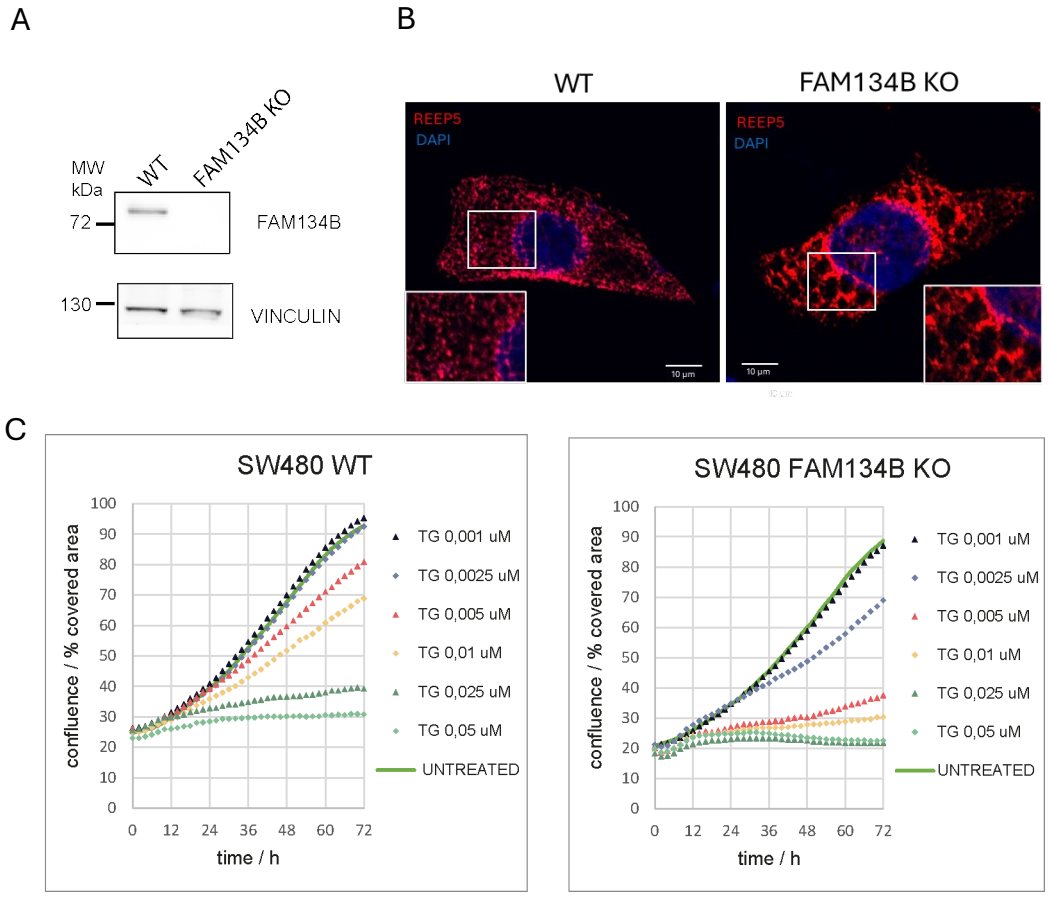

Figure 4. Generation of stable SW480 FAM134B KO cell line and response to TG treatment.
(A) Western blot confirming complete loss of FAM134B protein in SW480 FAM134B KO cells compared to WT. Vinculin was used as loading control. **(B)** Immunofluorescence staining of REEP5 (red) and nuclei (DAPI, blue) showing altered ER morphology in SW480 FAM134B KO cells. The ER network appears enlarged and less reticulated compared with the finely interconnected ER observed in WT cells. Scale bar 10 µm. **(C)** Dose–response curves of SW480 WT and FAM134B KO cells treated with increasing concentrations of Tapsigargin. Cell proliferation was monitored for 72 h using IncuCyte live-cell imaging, and confluence (% covered area) was used as an indicator of viability and growth

To further investigate the functional connection between FAM134B and SERCA2 (ATP2A2), identified as a FAM134B interactor in SW480 cells (Figure 4), we generated, via CRISPR Cas9 system, stable SW480 FAM134B knockout (KO) cell line. Western blot analysis confirmed the complete absence of FAM134B protein in FAM134B KO cells compared to the wild-type (WT) counterpart, validating the successful disruption of the gene (Figure 5A).

To examine the impact of FAM134B loss on ER organization, we performed immunofluorescence staining for REEP5. WT cells displayed a dense, continuous ER network surrounding the nucleus, while FAM134B KO cells exhibited a visibly enlarged (39) and less interconnected ER (Figure 5B). This phenotype is consistent with impaired ER remodeling and reduced membrane turnover, suggesting that FAM134B contributes to maintaining proper ER architecture (39).

Next, to evaluate the functional consequences of this alteration, we assessed cellular sensitivity to TG, a specific inhibitor of the SERCA pump, that induces ER stress by preventing Ca^{2+} re-uptake into the ER lumen (58). Both SW480 WT and FAM134B KO cells were treated with increasing concentrations of TG (0.001–0.05 μM) and monitored for 72 hours, with confluence used as a proxy for cell proliferation (Figure 5C).

In WT cells, TG treatment caused a dose-dependent reduction in proliferation, with marked inhibition at concentrations ≥0.01 μM. Differently, FAM134B KO cells showed a stronger sensitivity to TG even at lower doses, exhibiting slower growth and reduced viability over time. This enhanced vulnerability indicates that loss of FAM134B compromises cellular resistance to ER stress and Ca^{2+} imbalance, reinforcing the idea that FAM134B plays a protective role in buffering SERCA-dependent Ca^{2+} perturbations and preserving ER homeostasis (59)

Overall, these data confirm that FAM134B is required for proper ER morphology and stress adaptation in SW480 cells. The increased susceptibility of FAM134B-deficient cells to SERCA inhibition supports a functional link between ER-phagy and Ca^{2+} handling, which will be further explored in the following experiments.

6. Loss of FAM134B enhances ER Ca^{2+} release and mitochondrial Ca^{2+} uptake

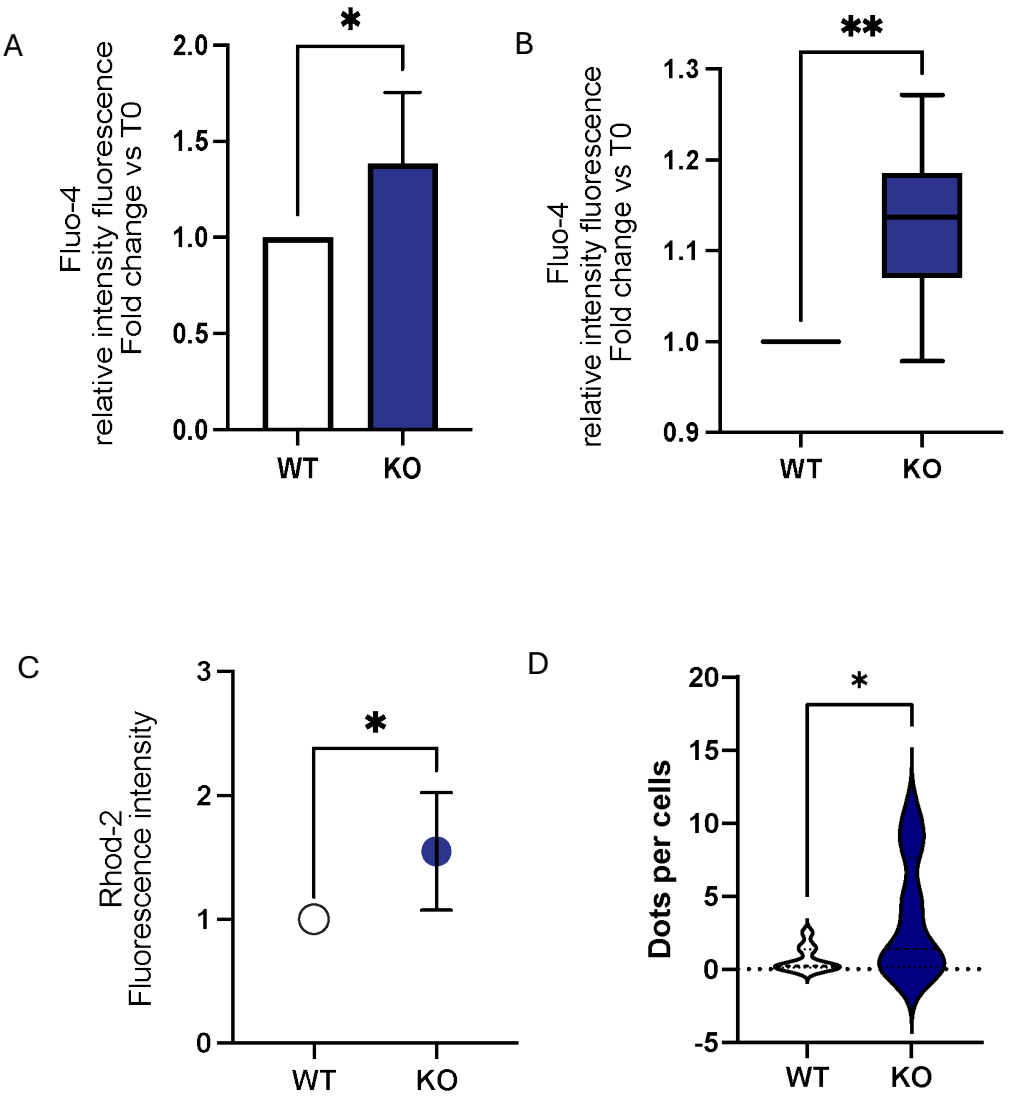

Figure 6. FAM134B modulates ER–mitochondria Ca^{2+} fluxes under TG treatment.
(A) Cytosolic Ca^{2+} release (Fluo-4) in WT and FAM134B KO cells after TG treatment. **(B)** Cytosolic Ca^{2+} release (Fluo-4) in WT and FAM134B KO cells in Ca^{2+} free medium. **(C)** Mitochondrial Ca^{2+} levels measured with Rhod-2 upon TG treatment. **(D)** Quantification of ER–mitochondria contact sites by proximity ligation assay (PLA).

To better understand if FAM134B may influence Ca^{2+} homeostasis, we analyzed Ca^{2+} dynamics in SW480 WT and FAM134B KO cells treated with TG. By blocking SERCA, TG causes Ca^{2+} to leak out from the ER into the cytosol, allowing us to directly monitor ER Ca^{2+} release.

When we measured cytosolic Ca^{2+} using Fluo-4 (60), we observed a clear increase in fluorescence intensity in the FAM134B KO cells compared to WT (Figure 6A). This

indicates that, after SERCA inhibition, more Ca^{2+} is released from the ER in the absence of FAM134B.

To clarify whether this increase depended on extracellular Ca^{2+} influx or truly reflected release from internal stores, we repeated the experiment in Ca^{2+} free medium. Interestingly, even without extracellular Ca^{2+}, FAM134B KO cells still showed a stronger Fluo-4 signal than WT (Figure 6B). This means that the Ca^{2+} rise is not due to entry from outside, but instead originates from intracellular stores, specifically from the ER.

Because Ca^{2+} released from the ER is often transferred directly to mitochondria through specialized membrane contact sites (Mitochondria Associated Membranes MAMs) (40), we next asked whether this flux affected mitochondrial Ca^{2+} content. Using Rhod-2, a mitochondrial Ca^{2+} indicator, (61) we found that FAM134B KO cells displayed higher mitochondrial Ca^{2+} accumulation than WT following TG treatment (Figure 6C). This suggests that Ca^{2+} released from the ER in FAM134B KO cells is efficiently transferred to mitochondria, reinforcing the idea of an altered ER–mitochondria buffering.

To support this, we performed a proximity ligation assay (PLA) to quantify ER–mitochondria contact sites, the regions where Ca^{2+} exchange physically occurs (62). The number of contacts was significantly higher in FAM134B KO cells compared to WT (Figure 6D), indicating that loss of FAM134B promotes the formation or stabilization of ER- mitochondria interfaces.

Overall, these results reveal that FAM134B depletion enhances ER Ca^{2+} release and increases Ca^{2+} transfer to mitochondria. Even when extracellular Ca^{2+} is removed, FAM134B KO cells maintain a stronger Ca^{2+} signal, confirming that FAM134B regulates the balance of intracellular Ca^{2+} fluxes.

Taken together, the data suggest that FAM134B acts as a key modulator of ER–mitochondria communication, possibly functioning as a negative regulator of Ca^{2+} transfer between the two organelles. In its absence, ER Ca^{2+} is released more readily, more contact sites form, and mitochondria take up larger Ca^{2+} amounts, potentially predisposing cells to stress or mitochondrial dysfunction (43).

7. Enhanced ER–mitochondria Ca^{2+} flux causes mitochondrial dysfunction in FAM134B KO cells

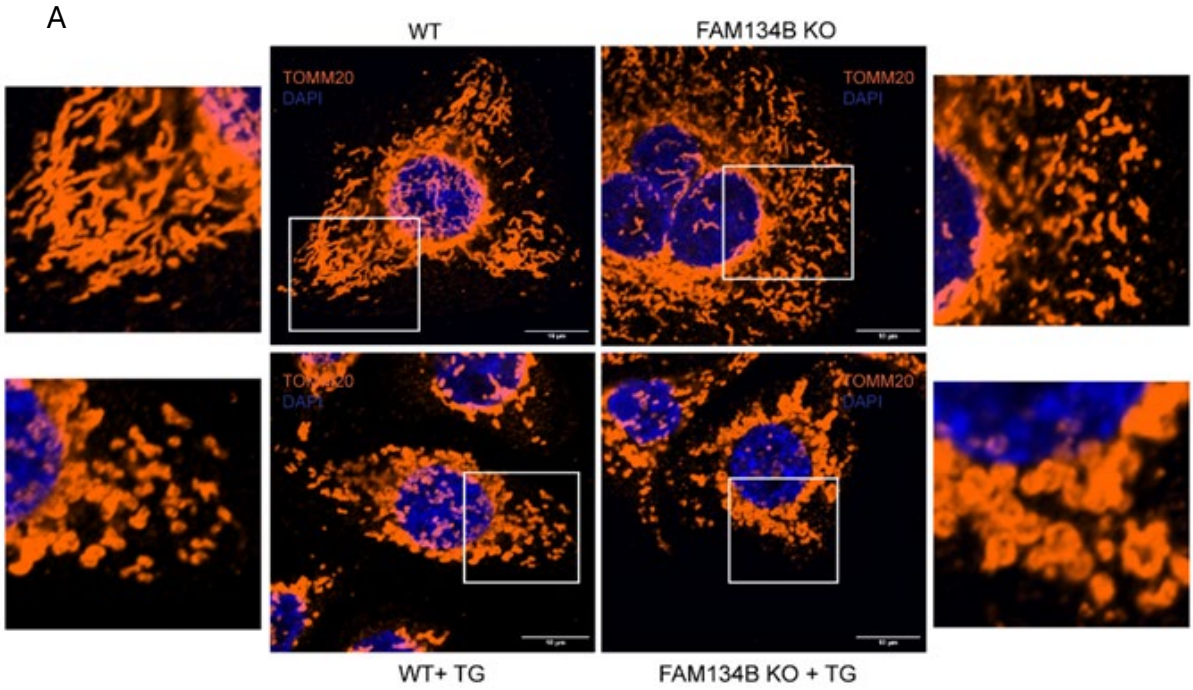

Figure 7. FAM134B loss induces mitochondrial fragmentation and reduces respiratory capacity under ER stress.
(A) Immunofluorescence staining of TOMM 20 showing mitochondrial morphology in SW480 WT and FAM134B KO cells, with and without TG treatment. Insets highlight representative structures. Scale bar 10 µm. **(B)** Quantification of maximal respiration (OCR) measured by Seahorse analysis. FAM134B KO cells exhibit reduced respiratory capacity compared to WT, and TG treatment further decreases mitochondrial performance in both genotypes.

Building on the observation that FAM134B deletion enhances ER Ca^{2+} release and increases ER–mitochondria coupling (Figure 6), we next examined whether these alterations impact mitochondrial organization and function.

Mitochondrial morphology is highly sensitive to intracellular Ca^{2+} fluctuations and ER stress, with sustained Ca^{2+} transfer often promoting fission and structural remodeling (40). To assess whether the increased Ca^{2+} flux observed in FAM134B-deficient cells

affects mitochondrial integrity, we analyzed mitochondrial morphology by immunofluorescence staining for TOMM20 (Figure 8A).

In SW480 WT cells, mitochondria displayed an elongated and interconnected filamentous network, characteristic of healthy and functionally active mitochondria. In contrast, FAM134B KO cells exhibited a more fragmented and punctate mitochondrial pattern, suggesting a disruption of the mitochondrial network integrity. Following TG treatment, which triggers ER Ca^{2+} release and induces ER stress, both WT and FAM134B KO cells showed a marked morphological rearrangement of mitochondria, forming rounded and swollen structures. However, these circular and enlarged mitochondrial profiles were more pronounced in the FAM134B KO cells, consistent with their higher intracellular Ca^{2+} levels and altered ER-mitochondria communication.

Because mitochondrial morphology is often linked to its functional state (41), we next examined whether the bioenergetic activity of mitochondria was also affected. Using the Seahorse XF assay, we measured mitochondrial respiration. As shown in Figure 7B, maximal respiration was significantly reduced in FAM134B KO cells compared to WT, indicating impaired mitochondrial performance. TG treatment further exacerbated this defect in both genotypes, with the FAM134B KO treated with TG displaying the lowest respiratory capacity.

Taken together, these results show that loss of FAM134B not only alters mitochondrial morphology but also compromises mitochondrial function, particularly under conditions of ER stress induced by SERCA inhibition. The increased Ca^{2+} transfer from the ER to mitochondria in FAM134B KO cells may contribute to mitochondrial Ca^{2+} overload, leading to fragmentation and reduced oxidative capacity.

These results position FAM134B as a key regulator of ER–mitochondria crosstalk, maintaining Ca^{2+} balance and sustaining mitochondrial bioenergetic integrity.

Together with the data from Figures 5-6, these findings indicate that FAM134B regulates ER–mitochondria Ca^{2+} exchange to preserve mitochondrial structure and energy production.

In the next section, we assessed whether these structural and metabolic perturbations translate into increased susceptibility to stress-induced apoptosis, further defining the protective role of FAM134B in maintaining cellular homeostasis

8. FAM134B depletion promotes apoptosis upon SERCA inhibition

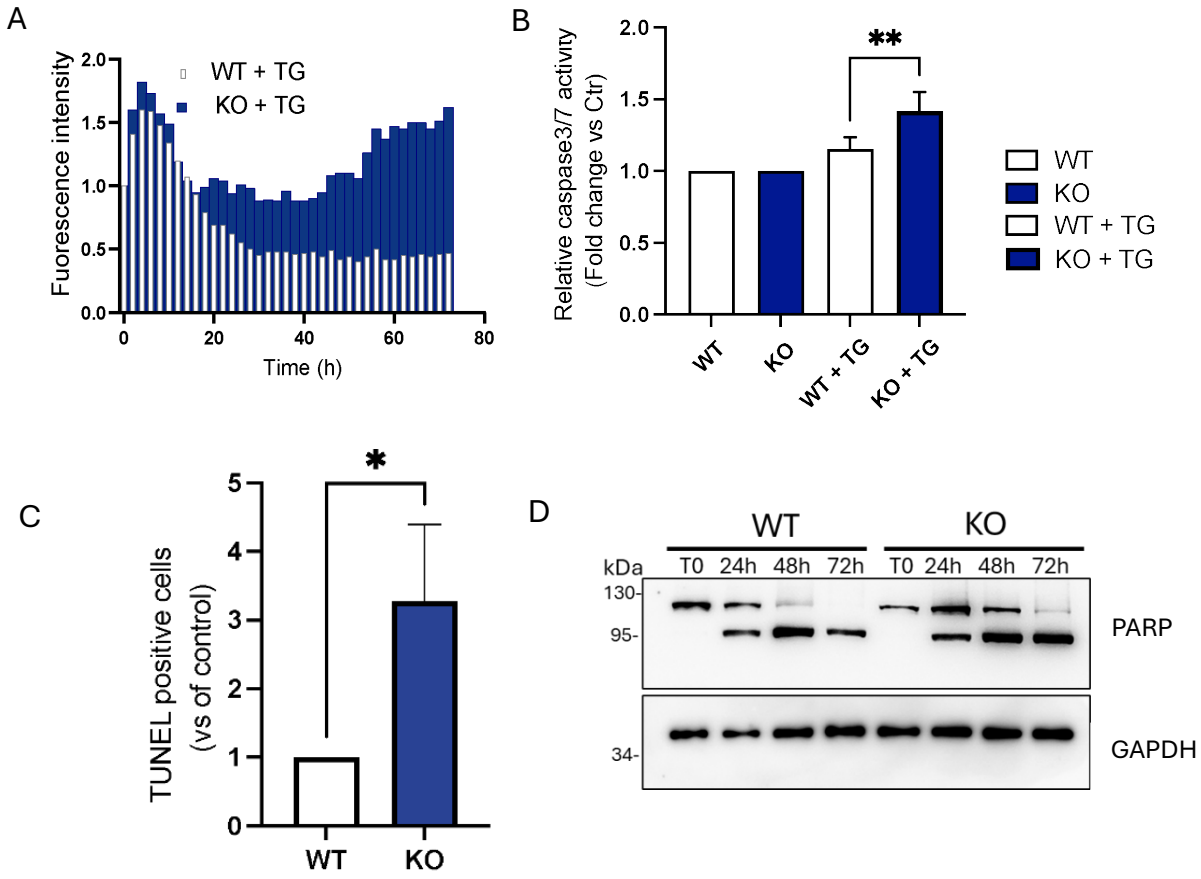

Figure 8. FAM134B loss promotes apoptosis.
(A) Live-cell monitoring of caspase-3/7 activation using IncuCyte imaging over 72 h following 10 nM TG treatment. **(B)** Endpoint caspase-3/7 activity assay confirms a significant increase in caspase activation in FAM134B KO cells compared to WT after 48 h of TG 10 nM exposure. **(C)** TUNEL assay showing a higher percentage of apoptotic (TUNEL-positive) cells in FAM134B KO versus WT following 10 nM TG treatment for 48 h. **(D)** Western blot analysis of PARP showing the decrease of full-length PARP (~116 kDa) and accumulation of its cleaved fragment (~89 kDa). GAPDH was used as loading control.

Given that FAM134B KO cells accumulate higher Ca^{2+} levels within mitochondria upon TG treatment, we next asked whether this excessive Ca^{2+} might affect cell survival. Ca^{2+} overload in mitochondria is known to promote the opening of the mitochondrial permeability transition pore (mPTP), loss of membrane potential, and activation of apoptotic pathways (43).

To address this, we monitored apoptosis in SW480 WT and FAM134B KO cells treated with TG. Using the IncuCyte live-cell imaging system coupled with a caspase-3/7 activation probe, we observed that apoptosis progressively increased over time, and

that FAM134B KO cells displayed a significantly higher apoptotic signal compared to WT cells (Figure 8A).

To confirm these results using an independent method, caspase-3/7 activity was quantified using a commercial fluorometric kit. Consistent with the live-imaging data, FAM134B KO cells displayed a marked increase in caspase activity compared with WT after TG exposure (Figure 8B).

We next analyzed apoptosis at a later stage through a TUNEL assay, which revealed a significantly higher percentage of apoptotic nuclei in FAM134B KO cells compared with WT (Figure 8C). Finally, PARP cleavage, a hallmark of executioner caspase activity (63), was examined by Western blot. WT cells exhibited a gradual reduction of full-length PARP (~116 kDa) and appearance of the cleaved 89 kDa form over time, whereas FAM134B KO cells showed an earlier and more intense accumulation of the cleaved fragment (Figure 8D).

Together, these results indicate that FAM134B deficiency sensitizes cells to ER stress-induced apoptosis. The enhanced Ca^{2+} transfer from the ER to mitochondria in FAM134B KO cells likely contributes to mitochondrial Ca^{2+} overload, leading to mitochondrial dysfunction and activation of the intrinsic apoptotic pathway. These data suggest that FAM134B plays a protective role, maintaining Ca^{2+} homeostasis and limiting apoptosis during ER stress.

Given these results, we next investigated whether re-expression of FAM134B could rescue the observed phenotypes, restoring Ca^{2+} balance, apoptosis and mitochondrial respiration.

9. FAM134B reconstitution re-establishes Ca^{2+} balance and metabolic integrity

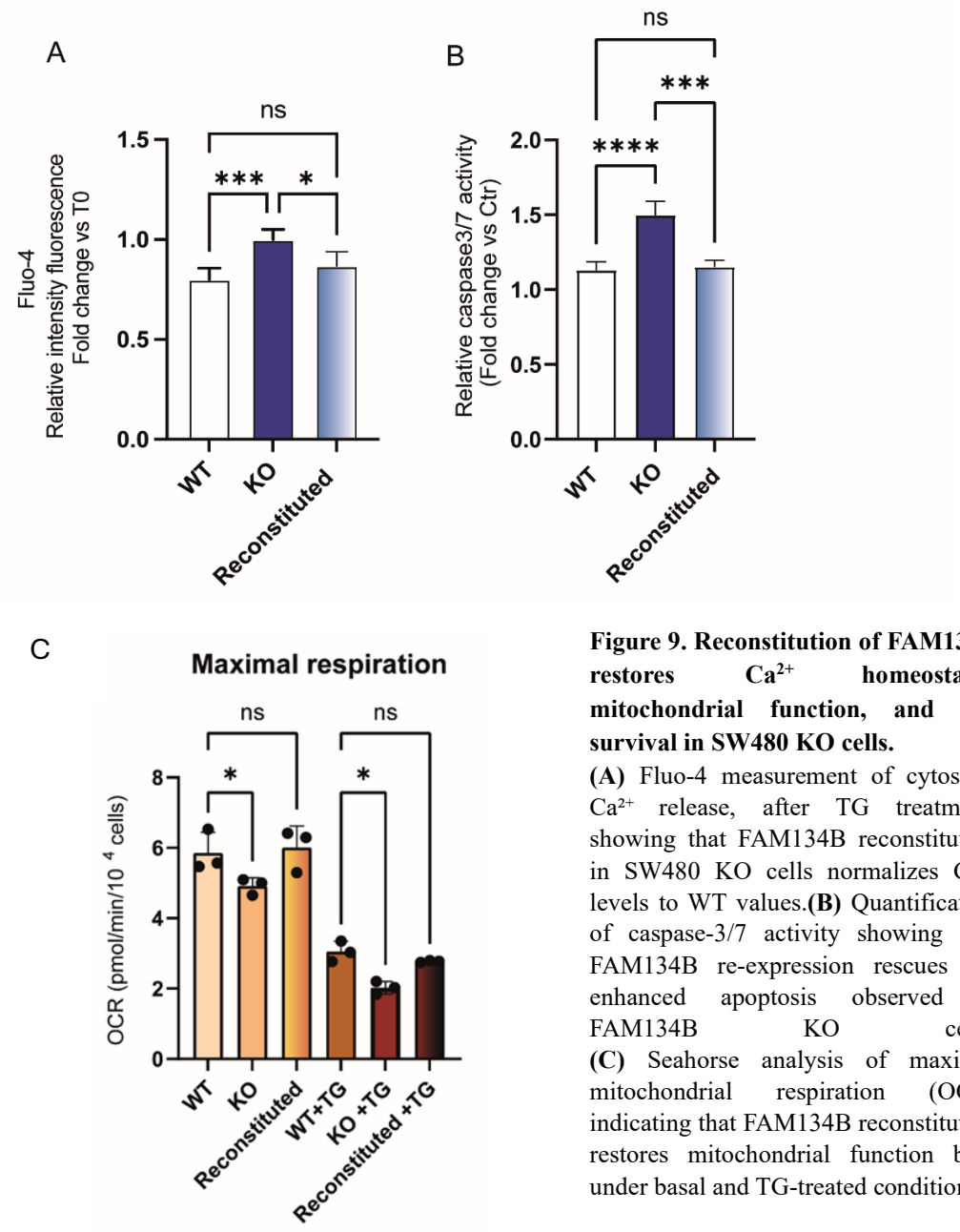

Figure 9. Reconstitution of FAM134B restores Ca^{2+} homeostasis, mitochondrial function, and cell survival in SW480 KO cells.
(A) Fluo-4 measurement of cytosolic Ca^{2+} release, after TG treatment, showing that FAM134B reconstitution in SW480 KO cells normalizes Ca^{2+} levels to WT values.**(B)** Quantification of caspase-3/7 activity showing that FAM134B re-expression rescues the enhanced apoptosis observed in FAM134B KO cells. **(C)** Seahorse analysis of maximal mitochondrial respiration (OCR) indicating that FAM134B reconstitution restores mitochondrial function both under basal and TG-treated conditions

To confirm that the phenotypes observed in FAM134B KO cells were specifically due to the loss of FAM134B and not to off-target effects, we generated a reconstituted cell line by stably re-expressing wild-type FAM134B in the KO background. This allowed us to evaluate whether restoring FAM134B expression could rescue the alterations previously observed in Ca^{2+} signaling, apoptosis, and mitochondrial respiration.

We first assessed cytosolic Ca^{2+} levels using the Fluo-4 probe after TG treatment. As shown in Figure 9A, FAM134B KO cells exhibited a significant increase in Fluo-4 fluorescence compared to WT, consistent with an enhanced ER Ca^{2+} release.

Importantly, FAM134B reconstitution normalized this signal, restoring Ca^{2+} levels close to those of the WT cells. This confirms that FAM134B directly contributes to maintaining intracellular Ca^{2+} homeostasis during ER stress.

Next, we analyzed caspase-3/7 activation as a marker of apoptosis under the same experimental conditions. In agreement with previous results, FAM134B KO cells showed a marked increase in caspase activation following TG treatment, while reconstituted cells displayed significantly reduced caspase activity, comparable to WT levels (Figure 9B). These findings demonstrate that re-expression of FAM134B protects cells from excessive apoptosis induced by ER Ca^{2+} dysregulation.

Finally, we examined mitochondrial respiration using the Seahorse XF assay. In both basal and TG-treated conditions, FAM134B KO cells exhibited reduced maximal respiration compared to WT, confirming mitochondrial dysfunction. Strikingly, reconstitution of FAM134B rescued mitochondrial performance, restoring oxygen consumption to levels indistinguishable from WT (Figure 9C).

Altogether, these data conclusively demonstrate that FAM134B plays a central role in coordinating ER-mitochondria Ca^{2+} fluxes, preserving mitochondrial function, and preventing ER stress-induced apoptosis. The complete rescue of Ca^{2+} handling, caspase activation, and respiratory capacity upon FAM134B re-expression confirms that the phenotypes observed in FAM134B KO cells are directly dependent on the absence of FAM134B.

Together, our findings reveal that FAM134B is a key regulator of ER–mitochondria communication and Ca^{2+} homeostasis. Loss of FAM134B leads to excessive Ca^{2+} release from the ER, increased Ca^{2+} transfer to mitochondria, and changes in mitochondrial structure and function. Therefore, FAM134B-deficient cells exhibit reduced respiratory capacity and a higher susceptibility to ER stress-induced apoptosis.

Importantly, re-expression of FAM134B fully rescues these phenotypes, restoring normal Ca^{2+} fluxes, mitochondrial performance, and cell survival. These results demonstrate that FAM134B plays a crucial protective role in maintaining intracellular Ca^{2+} balance and mitochondrial integrity during stress conditions.

Altogether, the data support a model in which FAM134B coordinates ER-mitochondria crosstalk to preserve cellular homeostasis, linking ER-phagy, Ca^{2+} signaling, and metabolic fitness in CRC cells.

Discussion

FAM134B was originally identified in colorectal cancer (CRC) under the name JK-1, as one of the first genes upregulated in tumor tissues compared with adjacent non-tumorous mucosa (64). Since then, FAM134B has been recognized as a critical receptor for ER-phagy, the selective autophagic turnover of ER membranes, which is essential for maintaining ER integrity and proteostasis (12,39). Despite its discovery in CRC, the precise role of FAM134B in this cancer type has remained poorly understood. In this work, we sought to elucidate both the molecular and functional contribution of FAM134B in CRC, focusing on how its loss affects ER homeostasis, Ca^{2+} signaling, mitochondrial function, and cell fate.

We first analyzed a panel of CRC-derived epithelial cell lines to evaluate the expression of FAM134B together with canonical markers of macro-autophagy and ER-phagy. Western blot analysis of LC3 and p62, combined with live-cell imaging using the tandem RFP-GFP-KDEL reporter, revealed that both general autophagy and ER-phagy vary significantly across different CRC models. These differences indicate that each cell line engages the autophagic machinery to a distinct extent, reflecting cell type-specific adaptations to stress and metabolic demands. Because FAM134B acts as an ER-phagy receptor, we reasoned that its interactome might also differ among these models, potentially uncovering stage or context-specific regulatory partners.

Immunoprecipitation followed by mass spectrometry (IP-MS/MS) confirmed that the set of interacting proteins indeed varies across the CRC lines, with only a few shared components. Remarkably, among these common interactors, we consistently identified ATP2A2 (SERCA2), the ER Ca^{2+} ATPase responsible for refilling luminal Ca^{2+} stores and maintaining intracellular Ca^{2+} balance (65). This observation raised a compelling hypothesis: since SERCA regulates ER Ca^{2+} homeostasis and FAM134B drives ER turnover, a functional connection between FAM134B and Ca^{2+} signaling could exist. To test this hypothesis, we pharmacologically inhibited SERCA with TG, an established ER stressor that blocks Ca^{2+} reuptake and induces Ca^{2+} release from the ER (58), and we compared Ca^{2+} dynamics in wild-type versus FAM134B-deficient cells.

At this stage, we focused our investigation on a single CRC line, SW480, for both biological and technical reasons. SW480 cells harbor a characteristic mutational profile with activating mutations in *KRAS* (G12V) and truncating *APC* mutations, together with double missense mutations in *TP53* (R273H, P309S) that confer gain-of-function properties and alter stress responses (57,66). This background makes

SW480 a highly relevant model for dissecting autophagy, ER stress, and apoptotic pathways. In addition, SW480 cells display robust autophagic flux, respond reproducibly to SERCA inhibition, and are amenable to stable knockout and rescue approaches, thus providing an ideal platform for mechanistic studies.

Loss of FAM134B in SW480 cells led to a visibly enlarged and disorganized ER network, consistent with impaired ER-phagy and accumulation of undegraded ER membranes (18,39). Functionally, FAM134B-knockout cells exhibited an enhanced cytosolic Ca^{2+} release upon TG treatment, even in the absence of extracellular Ca^{2+}, confirming that the released Ca^{2+} originated from intracellular stores. Concomitantly, we observed increased mitochondrial Ca^{2+} accumulation and a rise in ER-mitochondria contact sites (MAMs), suggesting tighter inter-organelle coupling (67). These findings indicate that FAM134B deficiency promotes ER Ca^{2+} leakage and its transfer to mitochondria, likely via the IP_3R-GRP75-VDAC/MCU complex that mediates Ca^{2+} exchange between the two organelles (67).

Sustained mitochondrial Ca^{2+} overload is a well-established trigger of mitochondrial permeability transition and apoptosis (42,43). In line with this, our data revealed that FAM134B-deficient cells display fragmented and rounded mitochondria, together with a marked decrease in maximal respiratory capacity measured through Seahorse metabolic assays. These changes reflect a loss of mitochondrial fitness and bioenergetic collapse, linking FAM134B deficiency to Ca^{2+}-dependent mitochondrial dysfunction.

Apoptotic assays further confirmed that FAM134B loss sensitizes cells to Ca^{2}-mediated death. Upon TG treatment, FAM134B-knockout cells showed increased caspase-3/7 activation, higher TUNEL positivity, and more pronounced PARP cleavage compared with wild-type controls. This phenotype is consistent with the notion that uncontrolled ER Ca^{2+} release and mitochondrial overload activate the intrinsic apoptotic pathway (43). Importantly, re-expression of FAM134B in knockout cells completely restored the wild-type phenotype, normalizing Ca^{2+} fluxes, mitochondrial respiration, and survival, thereby confirming that these effects arise directly from FAM134B loss.

Collectively, our results support a model in which FAM134B coordinates ER quality control and Ca^{2+} homeostasis. By ensuring SERCA-dependent Ca^{2+} refilling and proper ER turnover, FAM134B prevents pathological Ca^{2+} leakage, excessive ER–mitochondria tethering, and the ensuing mitochondrial dysfunction. In its absence, this

balance collapses, leading to Ca^{2+} dysregulation, energetic stress, and apoptosis. These findings extend the functional spectrum of FAM134B beyond its canonical role in ER-phagy and position it as a molecular safeguard that integrates membrane remodeling and Ca^{2+} signaling.

From a translational perspective, our data suggest that the FAM134B-SERCA-Ca^{2+} axis represents a potential therapeutic vulnerability in CRC. SERCA inhibitors such as TG and its tumor-activated prodrug mipsagargin (G-202) are currently under clinical evaluation (68). Our results imply that CRC cells with reduced FAM134B expression might be particularly sensitive to these Ca^{2+}-overload-based strategies. Conversely, interventions aimed at restoring FAM134B expression or enhancing ER-phagy could help preserve Ca^{2+} balance and protect against mitochondrial stress.

In conclusion, this study identifies FAM134B as a key integrator of ER-phagy, Ca^{2+} homeostasis, and cell survival. Its dual role in organelle turnover and Ca^{2+} regulation provides a new mechanistic framework for understanding ER-mitochondria communication and opens perspectives for the development of targeted therapeutic strategies in CRC.

References

1. Ohsumi Y. Historical landmarks of autophagy research. Cell Res. 2014 Jan;24(1):9–23.

2. Levine B, Kroemer G. Autophagy in the pathogenesis of disease. Cell. 2008 Jan 11;132(1):27–42.

3. Mizushima N, Yoshimori T, Levine B. Methods in mammalian autophagy research. Cell. 2010 Feb 5;140(3):313–26.

4. Li W wen, Li J, Bao J ku. Microautophagy: lesser-known self-eating. Cell Mol Life Sci CMLS. 2012 Apr;69(7):1125–36.

5. Kaushik S, Cuervo AM. Chaperone-mediated autophagy: a unique way to enter the lysosome world. Trends Cell Biol. 2012 Aug;22(8):407–17.

6. Gatica D, Lahiri V, Klionsky DJ. Cargo recognition and degradation by selective autophagy. Nat Cell Biol. 2018 Mar;20(3):233–42.

7. Kim J, Kundu M, Viollet B, Guan KL. AMPK and mTOR regulate autophagy through direct phosphorylation of Ulk1. Nat Cell Biol. 2011 Feb;13(2):132–41.

8. Feng Y, He D, Yao Z, Klionsky DJ. The machinery of macroautophagy. Cell Res. 2014 Jan;24(1):24–41.

9. Yu L, McPhee CK, Zheng L, Mardones GA, Rong Y, Peng J, et al. Termination of autophagy and reformation of lysosomes regulated by mTOR. Nature. 2010 June 17;465(7300):942–6.

10. Li W, He P, Huang Y, Li YF, Lu J, Li M, et al. Selective autophagy of intracellular organelles: recent research advances. Theranostics. 2021;11(1):222–56.

11. Mochida K, Nakatogawa H. ER-phagy: selective autophagy of the endoplasmic reticulum. EMBO Rep. 2022 Aug 3;23(8):e55192.

12. Grumati P, Dikic I, Stolz A. ER-phagy at a glance. J Cell Sci. 2018 Sept 3;131(17):jcs217364.

13. Stolz A, Ernst A, Dikic I. Cargo recognition and trafficking in selective autophagy. Nat Cell Biol. 2014 June;16(6):495–501.

14. Bjørkøy G, Lamark T, Brech A, Outzen H, Perander M, Overvatn A, et al. p62/SQSTM1 forms protein aggregates degraded by autophagy and has a protective effect on huntingtin-induced cell death. J Cell Biol. 2005 Nov 21;171(4):603–14.

15. Novak I, Kirkin V, McEwan DG, Zhang J, Wild P, Rozenknop A, et al. Nix is a selective autophagy receptor for mitochondrial clearance. EMBO Rep. 2010 Jan;11(1):45–51.

16. Grumati P, Morozzi G, Hölper S, Mari M, Harwardt MLIE, Yan R, et al. Full length RTN3 regulates turnover of tubular endoplasmic reticulum via selective autophagy. eLife. 2017 June 15;6:e25555.

17. Smith MD, Harley ME, Kemp AJ, Wills J, Lee M, Arends M, et al. CCPG1 Is a Non-canonical Autophagy Cargo Receptor Essential for ER-Phagy and Pancreatic ER Proteostasis. Dev Cell. 2018 Jan 22;44(2):217-232.e11.

18. Reggio A, Buonomo V, Berkane R, Bhaskara RM, Tellechea M, Peluso I, et al. Role of FAM134 paralogues in endoplasmic reticulum remodeling, ER-phagy, and Collagen quality control. EMBO Rep. 2021 Sept 6;22(9):e52289.

19. Hetz C. The unfolded protein response: controlling cell fate decisions under ER stress and beyond. Nat Rev Mol Cell Biol. 2012 Jan 18;13(2):89–102.

20. Carreras-Sureda A, Pihán P, Hetz C. Calcium signaling at the endoplasmic reticulum: fine-tuning stress responses. Cell Calcium. 2018 Mar;70:24–31.

21. Gentile D, Esposito M, Grumati P. Metabolic adaption of cancer cells toward autophagy: Is there a role for ER-phagy? Front Mol Biosci. 2022;9:930223.

22. Stolz A, Grumati P. The various shades of ER-phagy. FEBS J. 2019 Dec;286(23):4642–9.

23. Buonomo V, Lohachova K, Reggio A, Cano-Franco S, Cillo M, Santorelli L, et al. Two FAM134B isoforms differentially regulate ER dynamics during myogenesis. EMBO J. 2025 Feb;44(4):1039–73.

24. Forrester A, De Leonibus C, Grumati P, Fasana E, Piemontese M, Staiano L, et al. A selective ER-phagy exerts procollagen quality control via a Calnexin-FAM134B complex. EMBO J. 2019 Jan 15;38(2):e99847.

25. Markowitz SD, Bertagnolli MM. Molecular origins of cancer: Molecular basis of colorectal cancer. N Engl J Med. 2009 Dec 17;361(25):2449–60.

26. Clevers H. At the crossroads of inflammation and cancer. Cell. 2004 Sept 17;118(6):671–4.

27. Fearon ER, Vogelstein B. A genetic model for colorectal tumorigenesis. Cell. 1990 June 1;61(5):759–67.

28. Vousden KH, Prives C. Blinded by the Light: The Growing Complexity of p53. Cell. 2009 May 1;137(3):413–31.

29. White E. The role for autophagy in cancer. J Clin Invest. 2015 Jan;125(1):42–6.

30. Amaravadi R, Kimmelman AC, White E. Recent insights into the function of autophagy in cancer. Genes Dev. 2016 Sept 1;30(17):1913–30.

31. Liu EY, Xu N, O'Prey J, Lao LY, Joshi S, Long JS, et al. Loss of autophagy causes a synthetic lethal deficiency in DNA repair. Proc Natl Acad Sci U S A. 2015 Jan 20;112(3):773–8.

32. Clinical significance of p53 protein expression and TP53 variation status in colorectal cancer | BMC Cancer | Full Text [Internet]. [cited 2025 Aug 21]. Available from: https://bmccancer.biomedcentral.com/articles/10.1186/s12885-022-10039-y

33. Hassin O, Nataraj NB, Shreberk-Shaked M, Aylon Y, Yaeger R, Fontemaggi G, et al. Different hotspot p53 mutants exert distinct phenotypes and predict outcome of colorectal cancer patients. Nat Commun. 2022 May 19;13(1):2800.

34. Mulcahy Levy JM, Thorburn A. Autophagy in cancer: moving from understanding mechanism to improving therapy responses in patients. Cell Death Differ. 2020 Mar;27(3):843–57.

35. Zhou H, Wang K, Wang M, Zhao W, Zhang C, Cai M, et al. ER-phagy in the Occurrence and Development of Cancer. Biomedicines. 2022 Mar 18;10(3):707.

36. Chipurupalli S, Ganesan R, Martini G, Mele L, Reggio A, Esposito M, et al. Cancer cells adapt FAM134B/BiP mediated ER-phagy to survive hypoxic stress. Cell Death Dis. 2022 Apr 18;13(4):357.

37. Wang H, Liu L, Gong H, Li H. Upregulation of FAM134B inhibits endoplasmic reticulum stress-related degradation protein expression and promotes hepatocellular carcinogenesis. J Cell Mol Med. 2024 Mar;28(5):e17964.

38. Fumagalli F, Noack J, Bergmann TJ, Cebollero E, Pisoni GB, Fasana E, et al. Translocon component Sec62 acts in endoplasmic reticulum turnover during stress recovery. Nat Cell Biol. 2016 Nov;18(11):1173–84.

39. Khaminets A, Heinrich T, Mari M, Grumati P, Huebner AK, Akutsu M, et al. Regulation of endoplasmic reticulum turnover by selective autophagy. Nature. 2015 June 18;522(7556):354–8.

40. Giorgi C, Agnoletto C, Bononi A, Bonora M, De Marchi E, Marchi S, et al. Mitochondrial calcium homeostasis as potential target for mitochondrial medicine. Mitochondrion. 2012 Jan;12(1):77–85.

41. Marchi S, Pinton P. The mitochondrial calcium uniporter complex: molecular components, structure and physiopathological implications. J Physiol. 2014 Mar 1;592(Pt 5):829–39.

42. Giorgi C, Baldassari F, Bononi A, Bonora M, De Marchi E, Marchi S, et al. Mitochondrial Ca(2+) and apoptosis. Cell Calcium. 2012 July;52(1):36–43.

43. Pinton P, Giorgi C, Siviero R, Zecchini E, Rizzuto R. Calcium and apoptosis: ER-mitochondria Ca2+ transfer in the control of apoptosis. Oncogene. 2008 Oct 27;27(50):6407–18.

44. Monteith GR, McAndrew D, Faddy HM, Roberts-Thomson SJ. Calcium and cancer: targeting Ca2+ transport. Nat Rev Cancer. 2007 July;7(7):519–30.

45. Almanza A, Carlesso A, Chintha C, Creedican S, Doultsinos D, Leuzzi B, et al. Endoplasmic reticulum stress signalling - from basic mechanisms to clinical applications. FEBS J. 2019 Jan;286(2):241–78.

46. White E. The role for autophagy in cancer. J Clin Invest. 2015 Jan;125(1):42–6.

47. Zhou H, Chen H, Luo K, Kong L, Li Y. Inhibition of autophagy enhances the sensitivity of ciclopirox olamine in human chronic myelogenous leukemia K562 cells. Int J Med Sci. 2025 Sept 12;22(15):4013–25.

48. Xiang Y, Lyu R, Hu J. Oligomeric scaffolding for curvature generation by ER tubule-forming proteins. Nat Commun. 2023 May 5;14:2617.

49. Dikic I, Elazar Z. Mechanism and medical implications of mammalian autophagy. Nat Rev Mol Cell Biol. 2018 June;19(6):349–64.

50. Huang X, Yao J, Liu L, Chen J, Mei L, Huangfu J, et al. S-acylation of p62 promotes p62 droplet recruitment into autophagosomes in mammalian autophagy. Mol Cell. 2023 Oct 5;83(19):3485-3501.e11.

51. Chino H, Hatta T, Natsume T, Mizushima N. Intrinsically Disordered Protein TEX264 Mediates ER-phagy. Mol Cell. 2019 June 6;74(5):909-921.e6.

52. Croucher DR, Iconomou M, Hastings JF, Kennedy SP, Han JZR, Shearer RF, et al. Bimolecular complementation affinity purification (BiCAP) reveals dimer-specific protein interactions for ERBB2 dimers. Sci Signal. 2016 July 12;9(436):ra69.

53. Leibovitz A, Stinson JC, McCombs WB, McCoy CE, Mazur KC, Mabry ND. Classification of human colorectal adenocarcinoma cell lines. Cancer Res. 1976 Dec;36(12):4562–9.

54. Ahmed D, Eide PW, Eilertsen IA, Danielsen SA, Eknæs M, Hektoen M, et al. Epigenetic and genetic features of 24 colon cancer cell lines. Oncogenesis. 2013 Sept;2(9):e71–e71.

55. Hassin O, Nataraj NB, Shreberk-Shaked M, Aylon Y, Yaeger R, Fontemaggi G, et al. Different hotspot p53 mutants exert distinct phenotypes and predict outcome of colorectal cancer patients. Nat Commun. 2022 May 19;13:2800.

56. Wangsa D, Braun R, Schiefer M, Gertz EM, Bronder D, Quintanilla I, et al. The evolution of single cell-derived colorectal cancer cell lines is dominated by the continued selection of tumor-specific genomic imbalances, despite random chromosomal instability. Carcinogenesis. 2018 July 30;39(8):993–1005.

57. Tomita N, Jiang W, Hibshoosh H, Warburton D, Kahn SM, Weinstein IB. Isolation and characterization of a highly malignant variant of the SW480 human colon cancer cell line. Cancer Res. 1992 Dec 15;52(24):6840–7.

58. Doan NTQ, Paulsen ES, Sehgal P, Møller JV, Nissen P, Denmeade SR, et al. Targeting thapsigargin towards tumors. Steroids. 2015 May;97:2–7.

59. Jaskulska A, Janecka AE, Gach-Janczak K. Thapsigargin—From Traditional Medicine to Anticancer Drug. Int J Mol Sci. 2020 Dec 22;22(1):4.

60. İpek ÖY, Abbas F, Sajidy H, Canepari M. Fast Neuronal Calcium Signals in Brain Slices Loaded With Fluo-4 AM Ester. Eur J Neurosci. 2025 Jan;61(1):e16657.

61. Fonteriz RI, de la Fuente S, Moreno A, Lobatón CD, Montero M, Alvarez J. Monitoring mitochondrial [Ca(2+)] dynamics with rhod-2, ratiometric pericam and aequorin. Cell Calcium. 2010 July;48(1):61–9.

62. Chakraborty S, Suresh S, Buch H, Panchapakesan A, Ranga U. Proximity Ligation Assay to Detect the Proximity Between Host Proteins and Viral Proteins of HIV-1. Methods Mol Biol Clifton NJ. 2024;2807:245–58.

63. Yoo L, Hong S, Shin KS, Kang SJ. PARP-1 regulates the expression of caspase-11. Biochem Biophys Res Commun. 2011 May 13;408(3):489–93.

64. Kasem K, Gopalan V, Salajegheh A, Lu CT, Smith RA, Lam AKY. *Gene JK1* (*FAM134B*) e cancro del colon-retto: uno studio pilota sulle alterazioni del numero di copie del gene e sulle correlazioni con i parametri clinico-patologici. Exp Mol Pathol. 2014 Aug 1;97(1):31–6.

65. Periasamy M, Huke S. SERCA pump level is a critical determinant of Ca(2+)homeostasis and cardiac contractility. J Mol Cell Cardiol. 2001 June;33(6):1053–63.

66. Comprehensive molecular characterization of human colon and rectal cancer | Nature [Internet]. [cited 2025 Aug 21]. Available from: https://www.nature.com/articles/nature11252

67. Peruzzo R, Costa R, Bachmann M, Leanza L, Szabò I. Mitochondrial Metabolism, Contact Sites and Cellular Calcium Signaling: Implications for Tumorigenesis. Cancers. 2020 Sept 10;12(9):2574.

68. Mahalingam D, Wilding G, Denmeade S, Sarantopoulas J, Cosgrove D, Cetnar J, et al. Mipsagargin, a novel thapsigargin-based PSMA-activated prodrug: results of a first-in-man phase I clinical trial in patients with refractory, advanced or metastatic solid tumours. Br J Cancer. 2016 Apr 26;114(9):986–94.

Acknowledgments

At the end of these four long and extraordinary years, there are many people I wish to thank.

First and foremost, Paolo Grumati, for giving me the opportunity to grow professionally, for his constant support, trust, and encouragement in pursuing my goals.
My heartfelt thanks also go to the amazing Grumati's group, who accompanied my moments of stress with laughter and many happy memories. A special thank you to Michele, Martina, and Lucia, who worked with me on this project, and to Viviana, who shared this experience with me from the very beginning.

I am deeply grateful to Alexandra Stolz, who hosted me in her lab during my research stay in Frankfurt and provided brilliant insights and suggestions for my project. This experience allowed me to grow scientifically and personally, thanks also to the invaluable support of Sara and Pablo, who made my stay in cold Frankfurt much more enjoyable.

To my colleagues (and friends), Federica, Alfonso, Lucia, Valentina, and Gennaro: knowing that you were always there helped me face the hardest moments with a smile, even when it wasn't easy.
A special mention goes to Iolanda Boffa, my desk mate and partner in countless adventures: thank you for sharing your exceptional knowledge, your humor, and those long working nights at TIGEM.

Beyond my "TIGEM family", I would like to thank my real family, my parents and my brother, for always being by my side and supporting me throughout this journey. A tender thank you to the guest stars of the family, Treppy, Fusino, and Ruotina, who kept me company during the writing of this thesis and brought me sweet moments of distraction.
And even though Nerino is no longer here, I know he's part of the club from afar.

My deepest gratitude goes to Armando, for believing in me more than anyone else, for giving me strength, serenity, and confidence, your presence has been essential in completing this journey.

I also wish to thank my dearest friends, who have shared my successes, dreams, and milestones over the years.
In particular Rosa, for guiding me with affection and wisdom in every professional choice; Francesca, who has shared my worries and joys since our university days; and Roberta, who always manages to be even happier than me when I reach a goal. Thanks to Sara and Sabina, who have been pillars of my life for more than twenty years, and to Mariarosaria, for the special bond we share despite the “distance”. Finally, but perhaps most importantly, Enia and Carla, my “TEDIO’S GIRLS”: thank you for being an example of strength and determination that inspired me throughout these years.

I hope I haven’t gone on too long, but I want to end by saying that this achievement is not only mine, it also belongs a little to all of you.
Thank you, from the bottom of my heart

Marianna

Ringraziamenti

Alla fine di questi quattro lunghi e straordinari anni, ci sono molte persone che desidero ringraziare.

Innanzitutto, Paolo Grumati, per avermi dato l'opportunità di crescere professionalmente, per il costante supporto, la fiducia e l'incoraggiamento nel raggiungere i miei obiettivi.
Un sincero grazie anche al fantastico Grumati's group, che ha saputo accompagnare i miei momenti di stress con tante risate e bellissimi ricordi. Un ringraziamento speciale a Michele, Martina e Lucia, che hanno lavorato con me a questo progetto, e a Viviana, che ha condiviso con me questa esperienza sin dall'inizio.

Un grazie di cuore va anche ad Alexandra Stolz, che mi ha ospitata nel suo laboratorio durante la mia esperienza a Francoforte e mi ha fornito preziosi e brillanti suggerimenti per il mio progetto.
Se questa esperienza mi ha permesso di crescere così tanto, è stato anche grazie al supporto scientifico e umano di Sara e Pablo, che hanno reso la mia permanenza nella fredda Francoforte molto più piacevole.

Un ringraziamento affettuoso ai miei colleghi (e amici) Federica, Alfonso, Lucia, Valentina e Gennaro: sapere che ci siete sempre stati mi ha aiutata ad affrontare i momenti difficili con un sorriso, anche quando non era facile.
Una menzione speciale va a Iolanda Boffa, la mia compagna di scrivania e di tante avventure: grazie per aver condiviso con me la tua straordinaria preparazione, la tua ironia e le infinite nottate di lavoro al TIGEM.

Oltre alla mia "famiglia TIGEM", voglio ringraziare la mia famiglia vera: i miei genitori e mio fratello, per avermi accompagnata e sostenuta in ogni fase di questo percorso.
Un tenero grazie anche alle guest stars della famiglia, Treppy, Fusino e Ruotina, che mi hanno tenuto compagnia durante la stesura di questa tesi, regalandomi momenti di dolce distrazione. E anche se Nerino non è più con noi, so che da lontano è comunque parte del club.

Un pensiero speciale ad Armando, per aver creduto in me più di chiunque altro, per avermi trasmesso forza, serenità e fiducia in me stessa: la tua presenza è stata fondamentale per portare a termine questo percorso.

Ringrazio anche le mie amiche di sempre, che da anni condividono con me successi, sogni e traguardi.
In particolare Rosa, che con affetto e saggezza mi ha sempre guidata nelle scelte professionali; Francesca, con cui condivido ansie, paure e gioie sin dai banchi dell'università; Roberta, che riesce a essere più felice di me ogni volta che raggiungo un traguardo.
Grazie anche a Sara e Sabina, pilastri della mia vita da più di vent'anni, e a Mariarosaria, per il legame speciale che ci unisce nonostante la "distanza".
Infine, ma non per importanza, Enia e Carla, le mie "TEDIO'S GIRLS": grazie per essere state un esempio di tenacia e determinazione, e per avermi ispirata durante questi anni.

Sperando di non essermi dilungata troppo, voglio concludere dicendo che questo traguardo non è solo il mio, ma anche un po' vostro.
Grazie di cuore a tutti.

Marianna